

# Planck Early Results: The Galactic Cold Core Population revealed by the first all-sky survey

Planck Collaboration: P. A. R. Ade<sup>68</sup>, N. Aghanim<sup>45</sup>, M. Arnaud<sup>55</sup>, M. Ashdown<sup>53,74</sup>, J. Aumont<sup>45</sup>, C. Baccigalupi<sup>66</sup>, A. Balbi<sup>27</sup>, A. J. Banday<sup>72,6,60</sup>, R. B. Barreiro<sup>50</sup>, J. G. Bartlett<sup>3,51</sup>, E. Battaner<sup>76</sup>, K. Benabed<sup>46</sup>, A. Benoît<sup>46</sup>, J.-P. Bernard<sup>72,6</sup>, M. Bersanelli<sup>25,40</sup>, R. Bhatia<sup>33</sup>, J. J. Bock<sup>51,7</sup>, A. Bonaldi<sup>36</sup>, J. R. Bond<sup>5</sup>, J. Borrill<sup>59,69</sup>, F. R. Bouchet<sup>46</sup>, F. Boulanger<sup>45</sup>, M. Bucher<sup>3</sup>, C. Burigana<sup>39</sup>, P. Cabella<sup>27</sup>, C. M. Cantalupo<sup>59</sup>, J.-F. Cardoso<sup>56,3,46</sup>, A. Catalano<sup>3,54</sup>, L. Cayón<sup>18</sup>, A. Challinor<sup>75,53,8</sup>, A. Chamballu<sup>43</sup>, R.-R. Chary<sup>44</sup>, L.-Y. Chiang<sup>47</sup>, P. R. Christensen<sup>63,28</sup>, D. L. Clements<sup>43</sup>, S. Colombi<sup>46</sup>, F. Couchot<sup>58</sup>, A. Coulais<sup>54</sup>, B. P. Crill<sup>51,64</sup>, F. Cuttaia<sup>39</sup>, L. Danese<sup>66</sup>, R. D. Davies<sup>52</sup>, R. J. Davis<sup>52</sup>, P. de Bernardis<sup>24</sup>, G. de Gasperis<sup>27</sup>, A. de Rosa<sup>39</sup>, G. de Zotti<sup>36,66</sup>, J. Delabrouille<sup>3</sup>, J.-M. Delouis<sup>46</sup>, F.-X. Désert<sup>42</sup>, C. Dickinson<sup>52</sup>, K. Dobashi<sup>14</sup>, S. Donzelli<sup>40,48</sup>, O. Doré<sup>51,7</sup>, U. Dörl<sup>60</sup>, M. Douspis<sup>45</sup>, X. Dupac<sup>32</sup>, G. Efstathiou<sup>75</sup>, T. A. Enßlin<sup>60</sup>, E. Falgarone<sup>54</sup>, F. Finelli<sup>39</sup>, O. Forni<sup>72,6</sup>, M. Frailis<sup>38</sup>, E. Franceschi<sup>39</sup>, S. Galeotta<sup>38</sup>, K. Ganga<sup>3,44</sup>, M. Giard<sup>72,6</sup>, G. Giardino<sup>33</sup>, Y. Giraud-Héraud<sup>3</sup>, J. González-Nuevo<sup>66</sup>, K. M. Górski<sup>51,78</sup>, S. Gratton<sup>53,75</sup>, A. Gregorio<sup>26</sup>, A. Gruppiso<sup>39</sup>, F. K. Hansen<sup>48</sup>, D. Harrison<sup>75,53</sup>, G. Helou<sup>7</sup>, S. Henrot-Versillé<sup>58</sup>, D. Herranz<sup>50</sup>, S. R. Hildebrandt<sup>7,57,49</sup>, E. Hivon<sup>46</sup>, M. Hobson<sup>74</sup>, W. A. Holmes<sup>51</sup>, W. Hovest<sup>60</sup>, R. J. Hoyland<sup>49</sup>, K. M. Huffenberger<sup>77</sup>, A. H. Jaffe<sup>43</sup>, G. Joncas<sup>11</sup>, W. C. Jones<sup>17</sup>, M. Juvela<sup>16</sup>, E. Keihänen<sup>16</sup>, R. Keskitalo<sup>51,16</sup>, T. S. Kisner<sup>59</sup>, R. Kneissl<sup>31,4</sup>, L. Knox<sup>20</sup>, H. Kurki-Suonio<sup>16,34</sup>, G. Lagache<sup>45</sup>, J.-M. Lamarre<sup>54</sup>, A. Lasenby<sup>74,53</sup>, R. J. Laureijs<sup>33</sup>, C. R. Lawrence<sup>51</sup>, S. Leach<sup>66</sup>, R. Leonardi<sup>32,33,21</sup>, C. Leroy<sup>45,72,6</sup>, M. Linden-Vørnle<sup>10</sup>, M. López-Caniego<sup>50</sup>, P. M. Lubin<sup>21</sup>, J. F. Macías-Pérez<sup>57</sup>, C. J. MacTavish<sup>53</sup>, B. Maffei<sup>52</sup>, N. Mandolesi<sup>39</sup>, R. Mann<sup>67</sup>, M. Maris<sup>38</sup>, D. J. Marshall<sup>72,6</sup>, P. Martin<sup>5</sup>, E. Martínez-González<sup>50</sup>, G. Marton<sup>30</sup>, S. Masi<sup>24</sup>, S. Matarrese<sup>23</sup>, F. Matthai<sup>60</sup>, P. Mazzotta<sup>27</sup>, P. McGehee<sup>44</sup>, A. Melchiorri<sup>24</sup>, L. Mendes<sup>32</sup>, A. Mennella<sup>25,38</sup>, S. Mitra<sup>51</sup>, M.-A. Miville-Deschênes<sup>45,5</sup>, A. Moneti<sup>46</sup>, L. Montier<sup>72,6</sup> \*, G. Morgante<sup>39</sup>, D. Mortlock<sup>43</sup>, D. Munshi<sup>68,75</sup>, A. Murphy<sup>62</sup>, P. Naselsky<sup>63,28</sup>, F. Nati<sup>24</sup>, P. Natoli<sup>27,2,39</sup>, C. B. Netterfield<sup>13</sup>, H. U. Nørgaard-Nielsen<sup>10</sup>, F. Novello<sup>45</sup>, D. Novikov<sup>43</sup>, I. Novikov<sup>63</sup>, S. Osborne<sup>71</sup>, F. Pajot<sup>45</sup>, R. Paladini<sup>70,7</sup>, F. Pasian<sup>38</sup>, G. Patanchon<sup>3</sup>, T. J. Pearson<sup>7,44</sup>, V.-M. Pelkonen<sup>44</sup>, O. Perdereau<sup>58</sup>, L. Perotto<sup>57</sup>, F. Perrotta<sup>66</sup>, F. Piacentini<sup>24</sup>, M. Piat<sup>3</sup>, S. Plaszczynski<sup>58</sup>, E. Pointecouteau<sup>72,6</sup>, G. Polenta<sup>2,37</sup>, N. Ponthieu<sup>45</sup>, T. Poutanen<sup>34,16,1</sup>, G. Prézeau<sup>7,51</sup>, S. Prunet<sup>46</sup>, J.-L. Puget<sup>45</sup>, W. T. Reach<sup>73</sup>, R. Rebolo<sup>49,29</sup>, M. Reinecke<sup>60</sup>, C. Renault<sup>57</sup>, S. Ricciardi<sup>39</sup>, T. Riller<sup>60</sup>, I. Ristorcelli<sup>72,6</sup>, G. Rocha<sup>51,7</sup>, C. Rosset<sup>3</sup>, M. Rowan-Robinson<sup>43</sup>, J. A. Rubiño-Martín<sup>49,29</sup>, B. Rusholme<sup>44</sup>, M. Sandri<sup>39</sup>, D. Santos<sup>57</sup>, G. Savini<sup>65</sup>, D. Scott<sup>15</sup>, M. D. Seiffert<sup>51,7</sup>, G. F. Smoot<sup>19,59,3</sup>, J.-L. Starck<sup>55,9</sup>, F. Stivoli<sup>41</sup>, V. Stolyarov<sup>74</sup>, R. Sudiwala<sup>68</sup>, J.-F. Sygnet<sup>46</sup>, J. A. Tauber<sup>33</sup>, L. Terenzi<sup>39</sup>, L. Toffolatti<sup>12</sup>, M. Tomasi<sup>25,40</sup>, J.-P. Torre<sup>45</sup>, V. Toth<sup>30</sup>, M. Tristram<sup>58</sup>, J. Tuovinen<sup>61</sup>, G. Umana<sup>35</sup>, L. Valenziano<sup>39</sup>, P. Vielva<sup>50</sup>, F. Villa<sup>39</sup>, N. Vittorio<sup>27</sup>, L. A. Wade<sup>51</sup>, B. D. Wandelt<sup>46,22</sup>, N. Ysard<sup>16</sup>, D. Yvon<sup>9</sup>, A. Zacchei<sup>38</sup>, S. Zahorecz<sup>30</sup>, and A. Zonca<sup>21</sup>

(Affiliations can be found after the references)

Preprint online version: November 12, 2021

## ABSTRACT

We present the statistical properties of the first version of the Cold Core Catalogue of Planck Objects (C3PO), in terms of their spatial distribution, temperature, distance, mass, and morphology. We also describe the statistics of the Early Cold Core Catalogue (ECC) that is a subset of the complete catalogue, and that contains only the 915 most reliable detections. ECC is delivered as a part of the Early Release Compact Source Catalogue (ERCSC). We have used the CoCoCoDeT algorithm to extract about 10 thousand cold sources. The method uses the IRAS 100  $\mu$ m data as a warm template that is extrapolated to the *Planck* bands and subtracted from the signal, leading to a detection of the cold residual emission. We have used cross-correlation with ancillary data to increase the reliability of our sample, and to derive other key properties such as distance and mass.

Temperature and dust emission spectral index values are derived using the fluxes in the IRAS 100  $\mu$ m band and the three highest frequency *Planck* bands. The range of temperatures explored by the catalogue spans from 7 K to 17 K, and peaks around 13 K. Data are not consistent with a constant value of the associated spectral index  $\beta$  over the all temperature range.  $\beta$  ranges from 1.4 to 2.8 with a mean value around 2.1, and several possible scenarios are possible, including  $\beta(T)$  and the effect of multiple temperature components folded into the measurements.

For one third of the objects the distances are obtained using various methods such as the extinction signature, or the association with known molecular complexes or Infra-Red Dark Clouds. Most of the detections are within 2 kpc in the Solar neighbourhood, but a few are at distances greater than 4 kpc. The cores are distributed over the whole range of longitude and latitude, from the deep Galactic plane, despite the confusion, to high latitudes ( $> 30^\circ$ ). The associated mass estimates derived from dust emission range from 1 to  $10^5$  solar masses. Using their physical properties such as temperature, mass, luminosity, density and size, these cold sources are shown to be cold clumps, defined as the intermediate cold sub-structures between clouds and cores. These cold clumps are not isolated but mostly organized in filaments associated with molecular clouds. The Cold Core Catalogue of Planck Objects (C3PO) is the first unbiased all-sky catalogue of cold compact objects and contains 10783 objects. It gives an unprecedented statistical view to the properties of these potential pre-stellar clumps and offers a unique possibility for their classification in terms of their intrinsic properties and environment.

**Key words.** Cold Cores, Galaxy, Source extraction

## 1. Introduction

The main difficulty in understanding star formation lies in the vast range of scales involved in the process. If star formation it-

\* Corresponding author = Ludovic.Montier@cesr.fr

self is the outcome of gravitational instability occurring in cold and dense structures at sub-parsec scales, the characteristics of these structures (usually called pre-stellar cores) depend on their large-scale environment, up to Galactic scales because their formation and evolution is driven by a complex coupling of self-gravity with cooling processes, turbulence and magnetic fields, to name a few. To progress in the understanding of star formation pre-stellar cores need to be observed, in a variety of environments. More importantly, broad surveys are required to address statistical issues, and probe theoretical predictions regarding the initial mass function (IMF) largely determined at the stage of fragmentation of pre-stellar cores.

Unfortunately, the properties of the pre-stellar cores are still poorly known mostly because of observational difficulties. The total number of Galactic pre-stellar cores is estimated to be around  $3 \times 10^5$  (Clemens et al. 1991) but most of them have so far escaped detection, simply because they are cold and immersed in warmer (therefore brighter) environments.

The thermal dust emission of nearby molecular clouds has been mapped from the ground in the millimeter and submillimeter ranges with instruments such as SCUBA, MAMBO, SIMBA, and Laboca. Because of limited sensitivity, but also the presence of the atmospheric fluctuations that call for beam-throw of at most a few arcmin, the studies have concentrated on the brightest and most compact regions that are already in an active phase of star formation. Thanks to sub-arcminute resolution, these observations (together with dedicated molecular line studies) have been the main source of information also on the structure of the pre-stellar cores (Motte et al. 1998; Curtis & Richer 2010; Hatchell et al. 2005; Enoch et al. 2006; Kauffmann et al. 2008).

Many compact clouds were detected as absorption features on photographic plates. A new population of thousands of cold dark clouds was discovered by observations of mid-infrared absorption towards the bright Galactic background (MSX and ISOGAL surveys; see Egan et al. 1998; Perault et al. 1996). The absorption studies are, however, strongly biased towards the low latitudes and do not directly provide information on the temperature of the detected sources. For a definitive study of the cold cloud cores, one must turn to high resolution observations in the submillimetre or millimetre range (Andre et al. 2000). The Bolocam Galactic Plane Survey (BGPS) is producing mm data for the central part of the Galactic plane (Aguirre et al. 2010). The first results suggest that at kpc distances, even with a half arcmin resolution, one is detecting mainly cluster forming clumps rather than cores that would produce, at most, a small multiple system (Dunham et al. 2010).

Balloon borne experiments have provided larger blind surveys of higher latitudes. PRONAOS discovered cold condensations also in cirrus-type clouds (Bernard et al. 1999; Dupac et al. 2003). Similarly, Archeops (Désert et al. 2008) detected hundreds of sources with temperatures down to 7 K. The latest addition to the balloon borne surveys is the BLAST experiment which has located several hundred submillimetre sources in Vulpecula (Chapin et al. 2008) and Vela (Netterfield et al. 2009; Olmi et al. 2009), including a number of cold and probably pre-stellar cores.

Since its launch in May 2009, the Herschel satellite has already provided hundreds of new detections of both starless and protostellar cores (André et al. 2010; Bontemps et al. 2010; Könyves et al. 2010; Molinari et al. 2010; Ward-Thompson et al. 2010). There is an intriguing similarity between the core mass function (CMF) derived from these data, and the IMF that need to be investigated in different environments, towards the inner Galaxy in particular. The Herschel studies will eventually cover a significant fraction of the Galactic mid-plane and the central

parts of the nearby star-forming clouds but cannot cover high Galactic latitudes where star formation is known to occur. In this endeavor the main challenge is how to locate the cores because, even with Herschel, detailed studies must be limited to a small fraction of the whole sky.

The *Planck*<sup>1</sup> satellite (Tauber et al. 2010) improves over the previous studies by providing an *all-sky* submillimetre/millimetre survey that has both the sensitivity and resolution needed for the detection of compact sources. The shortest wavelength channels of *Planck* cover the wavelengths around and longwards of the intensity maximum of the cold dust emission:  $\nu^2 B_\nu(T = 10\text{K})$  peaks close to  $300\mu\text{m}$  while, with a temperature of  $T \sim 6\text{K}$ , the coldest dust inside the cores has its maximum close to  $500\mu\text{m}$ . Combined with far-infrared data such as the IRAS survey, the data enable accurate determination of both the dust temperature and the spectral index. We use the *Planck* observations to search for Galactic cold cores, i.e. compact cloud cores with colour temperatures below 14 K. Because of the limited resolution, we are likely to detect mainly larger clumps inside which the cores are located. The cores will be pre-stellar objects before (or at the very initial stages) of the protostellar collapse, or possibly more evolved sources that still contain significant amounts of cold dust. The Cold Core Catalogue of Planck Objects (C3PO) which will be made public at the end of the *Planck* proprietary period, will be the first all-sky catalogue of cold cloud cores and clumps. It will reveal the locations where the next generations of stars will be born and will provide an opportunity to address a number of key questions related to Galactic star formation: What are the characteristics of this source population? How does the distribution of the cores/clumps correlate with the current star formation activity and the location of the molecular cloud rings and the spiral arms? How are the sources related to large-scale structures like the FIR loops, bubbles, shells, and filaments? Are there pre-stellar cores at high latitudes? How much do the core properties depend on their environment? Investigations such as these will help us understand the origin of the pre-stellar cores, the instabilities that initiate the collapse, and the roles of turbulence and magnetic fields. The catalogue will prove invaluable for follow-up studies to investigate in detail the internal properties of the individual sources.

In this paper we describe the general properties of the current cold cores catalogue that is based on data that the *Planck* satellite has gathered during its first two scans of the full sky. In particular, we will describe the statistics of the Early Cold Cores Catalogue (ECC) that is part of the recently published Planck Early Release Compact Source Catalogue (ERCSC Planck Collaboration 2011c). ECC forms a subset of the full C3PO and contains only the most secure detections of all the sources with colour temperatures below 14 K. The final version of C3PO will be published in 2013. For historical reasons, we use "Cold Cores" to designate the entries in the C3PO and in the ECC, and similarly in much of this paper. However, as this paper and the companion paper (Planck Collaboration 2011r, hereafter Paper II) demonstrate, most of these are more correctly described as "cold clumps", intermediate in their structure and

<sup>1</sup> *Planck* (<http://www.esa.int/Planck>) is a project of the European Space Agency (ESA) with instruments provided by two scientific consortia funded by ESA member states (in particular the lead countries France and Italy), with contributions from NASA (USA) and telescope reflectors provided by a collaboration between ESA and a scientific consortium led and funded by Denmark.

physical scale between a true pre-stellar core and a molecular cloud.

*Planck* (Tauber et al. 2010; Planck Collaboration 2011a) is the third generation space mission to measure the anisotropy of the cosmic microwave background (CMB). It observes the sky in nine frequency bands covering 30–857 GHz with high sensitivity and angular resolution from 31' to 5'. The Low Frequency Instrument LFI; (Mandolesi et al. 2010; Bersanelli et al. 2010; Mennella et al. 2011) covers the 30, 44, and 70 GHz bands with amplifiers cooled to 20 K. The High Frequency Instrument (HFI; Lamarre et al. 2010; Planck HFI Core Team 2011a) covers the 100, 143, 217, 353, 545, and 857 GHz bands with bolometers cooled to 0.1 K. Polarization is measured in all but the highest two bands (Leahy et al. 2010; Rosset et al. 2010). A combination of radiative cooling and three mechanical coolers produces the temperatures needed for the detectors and optics (Planck Collaboration 2011b). Two Data Processing Centers (DPCs) check and calibrate the data and make maps of the sky (Planck HFI Core Team 2011b; Zacchei et al. 2011). *Planck*'s sensitivity, angular resolution, and frequency coverage make it a powerful instrument for galactic and extragalactic astrophysics as well as cosmology. Early astrophysics results are given in *Planck* Collaboration, 2011h–z.

## 2. Source Extraction

### 2.1. Data Set

As cold cores are traced by their cold dust emission in the submillimetric bands, we use *Planck* channel maps of the HFI at 3 frequencies : 353, 545 and 857 GHz as described in detail in Planck HFI Core Team (2011b). The temperature maps at these frequencies are based on the first two sky surveys of *Planck*, provided in Healpix format (Górski et al. 2005) at nside=2048. We give here a very brief summary of the data reduction, cf Planck HFI Core Team (2011b) for further details. Raw data are first processed to produce cleaned timelines (TOI) and associated flags identifying various systematic effects. The data analysis includes application of a low-pass filter, removal and correction of glitches, conversion to absorbed power and decorrelation of thermal stage fluctuations. For the cold core detection, and more generally for source detection, Solar System objects (SSO) are identified in the TOI data using the publicly available Horizon ephemerides and an SSO flag is created to ensure that they are not projected onto the sky.

Focal plane reconstruction and beam-shape estimates are obtained using observations of Mars. Beams are described by an elliptical Gaussian parameterisation leading to FWHM  $\theta_s$  given in Table 2 of Planck HFI Core Team (2011b). The attitude of the satellite as a function of time is provided by the two star trackers installed on the *Planck* spacecraft. The pointing for each bolometer is computed by combining the attitude with the location of the bolometer in the focal plane reconstructed from Mars observations.

From the cleaned TOI and the pointing, channel maps have been made using bolometers at a given frequency. The path from TOI to maps in the HFI DPC is schematically divided into three steps, ring-making, destriping and map-making. The first step averages circles within a pointing period to make rings with higher signal-to-noise ratio taking advantage of the redundancy of observations provided by the *Planck* scanning strategy. The low amplitude  $1/f$  component is accounted for in a second step using a destriping technique. Finally, cleaned maps are produced using a simple co-addition of the rings.

The noise in the channel maps is essentially white with a mean standard deviation of  $1.4 \times 10^{-3}$ ,  $4.1 \times 10^{-3}$ ,  $1.4 \times 10^{-3}$  MJy/sr at 353, 545 and 857 GHz respectively (Planck HFI Core Team 2011b). The photometric calibration is performed either at the ring level using the CMB dipole, for the lower frequency channels, or at the map level using FIRAS data, for the higher frequency channels at 545 and 857 GHz. The absolute gain calibration of HFI *Planck* maps is known to better than 2% at 353 GHz and 7% at 545 and 857 GHz (see Table 2 in Planck HFI Core Team 2011b).

The detection algorithm requires the use of ancillary data to trace the warm component of the gas. Thus we combine *Planck* data with the IRIS all-sky data (Miville-Deschênes & Lagache 2005). The choice of the IRIS 100  $\mu$ m as the *warm template* is motivated by the following: (i) 100  $\mu$ m is very close to the peak frequency of a black body at 20 K, and traces the warm component of the Galaxy; (ii) the fraction of small grains at this wavelength remains very small and does not significantly the estimate of the emission from large grains that is extrapolated to longer wavelengths; (iii) the IRAS survey covers almost the entire sky (only 2 bands of  $\sim 2\%$  of the whole sky are missing); (iv) the resolution of the IRIS maps is similar to the resolution of *Planck* in the high frequency bands, i.e. around 4.5'. Using the map at 100  $\mu$ m as the *warm template* is, of course, not perfect, because a non-negligible fraction of the cold emission is still present at this frequency. This lowers the intensity in the *Planck* bands after removal of the extrapolated background. We will describe in detail, especially in Sect. 2.3, how we deal with this issue for the photometry of the detected cores.

All *Planck* and IRIS maps have been smoothed at the same resolution 4.5' before source extraction and photometry processing.

### 2.2. Source Extraction Method

We have applied the detection method described in Montier et al. 2010, known as *CoCoCoDeT* (standing for Cold Core Colour Detection Tool), on the combined IRIS plus *Planck* data set described in Sect. 2.1. This algorithm uses the colour properties of the objects to be detected to separate them from the background. In the case of cold cores, the method selects compact sources colder than the surrounding envelope and the diffuse Galactic background, that is at about 17 K (Boulanger et al. 1996) but can largely vary from one place to the other across the Galactic plane or at higher latitudes. This *Warm Background Subtraction* method is applied on each one of the three *Planck* maps, and consists of 6 steps:

1. for each pixel, the background colour is estimated as the median value of the *Planck* map divided by the 100  $\mu$ m map within a disc of radius 15' around the central pixel;
2. the *warm component* in a pixel at the *Planck* frequency is obtained by multiplying the estimate of the background colour with the value of the pixel in the 100  $\mu$ m map;
3. the *cold residual* map is computed by subtracting the *warm component* from the *Planck* map;
4. the local standard deviation around each pixel in the *cold residual* map is estimated in a radius of 30' using the so-called Median Absolute Deviation that ensures robustness against a high confusion level of the background and presence of other point sources within the same area;
5. a thresholding detection method is applied in the *cold residual* map to detect sources at a signal-to-noise ratio  $\text{SNR} > 4$ ;



6. final detections are defined as local maxima of the SNR constrained so that there is a minimum distance of  $5'$  between them.

This process is performed at each *Planck* band yielding individual catalogues at 857 GHz, 545 GHz and 353 GHz. The last step of the source extraction consists in merging these three independent catalogues requiring a detection in all three bands at  $\text{SNR} > 4$ . This step rejects spurious detections that are due to map artifacts associated with a single frequency (e.g. stripes or under-sampled features). It increases the robustness of the final catalogue, which contains 10783 objects.

We stress that no any other a-priori constraints are imposed on the size of the expected sources, other than the limited area on which the background colour is estimated. Thus the maximum scale of the C3PO objects is about  $12'$ . Note also that this *Warm Background Subtraction* method uses local estimates of the colour, identifying a relative rather than an absolute colour excess. Thus cold condensations embedded in cold regions can be missed, while in hot regions condensations may be detected that are not actually cold. A more detailed analysis in temperature is required to assess the nature of the objects.

### 2.3. Photometry

We have developed a dedicated algorithm to derive the photometry of the clump itself. The fluxes are estimated from the *cold residual* maps, instead of working on the initial maps where the clumps are embedded in their warm surrounding envelope. As already stressed above, the main issue is to perform the photometry on the IRIS  $100\ \mu\text{m}$  maps that also include a fraction of the cold emission. The flux of the source at  $100\ \mu\text{m}$  has to be well determined for two reasons: (1) an accurate estimate of the flux at this frequency is required because it constrains significantly the rest of the analysis (in terms of spectral density distribution (SED) and temperature); (2) an incorrect estimate of the flux at  $100\ \mu\text{m}$  will propagate through the *Planck* bands after removal of the extrapolated *warm component*. The main steps of the photometry processing are described in the following subsections. An illustration of this process is provided in Fig. B.5 of the associated Planck Early Paper on Cold Clumps describing in detail a sample of 10 sources (Planck Collaboration 2011r).

#### 2.3.1. Step1: Elliptical Gaussian fit

An elliptical Gaussian fit is performed on the  $1^\circ \times 1^\circ$  colour map 857 GHz divided by  $100\ \mu\text{m}$  centered on each C3PO object. This results in estimates of three parameters: major axis extension  $\sigma_{\text{Maj}}$ , minor axis extension  $\sigma_{\text{Min}}$  and position angle  $\psi$ . The relation between the extension  $\sigma$  and the FWHM  $\theta$  of a Gaussian is given by :

$$\sigma = \theta / \sqrt{8 \ln(2)} \quad (1)$$

If the elliptical Gaussian fit is indeterminate, a symmetrical Gaussian is assumed with a FWHM fixed to  $\theta = 4.5'$ , and the flag *Aper Forced* is set to on. In these cases, the source fluxes are severely underestimated at all frequencies. This flagged population contains 978 sources which are rejected from the physical analysis of Sect. 4, but not from the entire catalogue, which is used to assess the association with ancillary data (cf Sect. 3) and to study morphology at large scale (cf Sect. 5).

#### 2.3.2. Step2: $100\ \mu\text{m}$ photometry

The photometry on the  $100\ \mu\text{m}$  map is obtained by surface fitting, performed on local maps of  $1^\circ \times 1^\circ$  centered on each candidate. All components of the map are fitted as a whole: a polynomial surface of an order between three and six for the background; a set of elliptical Gaussians when other point sources are detected inside the local map; and a central elliptical Gaussian corresponding to the cold core candidate for which the elliptical shape is set by the parameters obtained during step 1. When the fit of the background is poor, i.e. a clear degeneracy is observed between the polynomial fit and the central Gaussian, we switch to a simple aperture photometry on the local map. Note that the aperture photometry is performed taking into account the elliptical shape of the cold core provided by step 1. In such cases (140 sources), the flag *Bad Sfit  $100\ \mu\text{m}$*  is set to on. Occasionally no counterpart at all is observed at  $100\ \mu\text{m}$ , when the cold core candidate is too faint or very cold, or the confusion of the Galactic background is too high. In such case, we are not able to derive any reliable estimate of the  $100\ \mu\text{m}$  flux of the core, so only an upper-limit can be provided. This upper limit is defined as three times the standard deviation of the *cold residual* map within a  $25'$  radius circle, and the flag *Upper  $100\ \mu\text{m}$*  is set to on. There are 2356 objects for which only an upper limit of the temperature is derived. This population represents a very interesting sub-sample of the whole catalogue, probably the coldest objects, but we do not have confidence in the physical properties derived from the *Planck* data and so it is excluded from the physical analysis.

#### 2.3.3. Step 3: $100\ \mu\text{m}$ correction

Once an estimate of the flux at  $100\ \mu\text{m}$  has been provided by steps 1 and 2, the *warm template* at  $100\ \mu\text{m}$  is corrected by removing an elliptical Gaussian corresponding to the flux of the central clump. This new *warm template* is then extrapolated and subtracted from the *Planck* maps to build the *cold residual* maps. When only an upper limit has been obtained at  $100\ \mu\text{m}$ , the *warm template* is not changed.

#### 2.3.4. Step 4: *Planck* bands photometry

Aperture photometry is performed on local *cold residual* maps centered on each candidate in the *Planck* bands, at 857 GHz, 545 GHz and 353 GHz. This aperture photometry takes into account the real extension of each object by integrating the signal inside the elliptical Gaussian constrained by the parameters obtained at step 1. The background is estimated by taking the median value on an annulus around the source. Nevertheless, in 229 cases, no positive estimate of the flux has been obtained, because of the presence of cold point sources that are too close or because the background is highly confused. These sources (for which the flag *PS Neg* is set to on) are simply removed from the physical analysis described in this paper.

### 2.4. Monte-Carlo Quality Assessment

To assess the quality of our photometry algorithm, we have performed a Monte-Carlo analysis. A total of 10000 simulated sources are randomly distributed over the whole sky in the IRIS and *Planck* maps. The sources are assumed to follow the emission of a modified black body with a temperature randomly,  $T$ , distributed between 6 K and 20 K, and an associated spectral index given by  $\beta = 11.5 \times T^{-0.66}$  within a 20% error bar, based

Quantity	Normal		<i>Bad Sfit</i> 100 $\mu\text{m}$		<i>Aper Forced</i>		<i>Upper 100<math>\mu\text{m}</math></i>	
	Bias (%)	1 $\sigma$ (%)	Bias(%)	1 $\sigma$ (%)	Bias(%)	1 $\sigma$ (%)	Bias (%)	1 $\sigma$ (%)
Flux at 100 $\mu\text{m}$	1.4	31.7	1.0	4.7	-58.1	14.1	117.1	190.0
Flux at 857 GHz	-5.0	6.2	3.9	3.2	-56.3	13.8	-11.0	6.0
Flux at 545 GHz	-3.6	6.4	3.7	3.7	-55.8	14.4	-9.0	6.0
Flux at 353 GHz	-5.0	7.3	2.4	4.7	-58.9	14.8	-10.0	6.7
FWHM	-0.6	16.2	30.9	27.7	-25.2	16.3	-6.7	15.3
Ellipticity	0.0	8.2	0.0	9.5	-	-	0.0	9.0
T	-4.2	5.2	-4.1	1.6	-6.5	3.8	0.4	16.0
$\beta$	9.8	7.3	10.5	2.4	11.2	6.7	2.7	18.7

**Table 1.** Statistics of the Monte-Carlo analysis performed to estimate the robustness of the photometry algorithm. The bias (expressed in %) is defined as the relative error between the median of the output distribution of the photometry algorithm and the injected input. The 1 $\sigma$  (expressed in %) represents the discrepancy around the most probable value of the output distribution. Those quantities are given in the various cases corresponding to the output flags provided by the algorithm. Statistics of the temperature and spectral index is also given here to show the impact of the observed error on fluxes.

Quantity	Normal		<i>Bad Sfit</i> 100 $\mu\text{m}$		<i>Aper Forced</i>		<i>Upper 100<math>\mu\text{m}</math></i>	
	Bias (%)	1 $\sigma$ (%)	Bias(%)	1 $\sigma$ (%)	Bias(%)	1 $\sigma$ (%)	Bias (%)	1 $\sigma$ (%)
Flux at 100 $\mu\text{m}$	11.5	44.3	0.8	8.4	-51.6	21.1	204.5	278.2
Flux at 857 GHz	-4.0	8.1	2.1	4.7	-58.3	20.1	-10.4	7.1
Flux at 545 GHz	-2.5	8.0	2.4	4.9	-57.4	21.3	-7.8	7.0
Flux at 353 GHz	-3.4	8.7	1.9	5.5	-59.3	21.3	-8.7	7.4
FWHM	0.0	18.1	31.0	31.1	-24.4	16.9	-5.2	17.6
Ellipticity	0.0	9.3	-0.5	9.2	-	-	0.1	10.4
T	-2.1	6.3	-3.2	1.8	-4.4	6.2	6.8	20.6
$\beta$	7.1	8.2	9.3	2.6	5.6	12.3	-4.9	20.4

**Table 2.** Same as Table 1 in the Galactic plane ( $|b| < 25^\circ$ ).

on the work done on Archeops data by Désert et al. (2008). The FWHM of the simulated sources spans from 4.5' to 7' with an ellipticity ranging from 0 to 0.87. The flux at 857 GHz is taken from 10 to 500 Jy following a logarithmic random distribution. The derived fluxes in all IRAS and *Planck* bands take into account the colour correction. We apply our complete process of photometry on this set of simulated data, and retrieve an estimate of all quantities (fluxes, FWHM, ellipticity) in the various cases described by the flags listed before (cf Fig. A.1). Statistical bias and 1 $\sigma$  errors are derived for all quantities and cases, and are listed in Table 1 and 2 for all-sky and  $|b| < 25^\circ$  respectively. We the temperature and spectral index estimates recovered at the end of the processing are also listed to illustrate the impact of the errors on the fluxes.

This Monte-Carlo analysis confirms, firstly, why sources with *Aper forced* set to on should be rejected from the physical study, since for these sources fluxes are systematically underestimated by about 60%. Sources with *Upper 100  $\mu\text{m}$*  set to on, for which only an upper limit at 100  $\mu\text{m}$  has been provided by the algorithm, the flux at 100  $\mu\text{m}$  is over-estimated by a factor of two, with an associated discrepancy that can reach a factor of three times the input value in regions close to the Galactic plane. Moreover the fluxes in the *Planck* bands are significantly biased to lower values, with a bias greater than the 1 $\sigma$  discrepancy. The resulting temperature estimate is, as expected, greater than the injected value and the uncertainties in the temperature and spectral index are around 20%. This illustrates the limitations on any physical conclusions that could be drawn from this population of sources. When a bad fit of the 100  $\mu\text{m}$  background has been obtained, *Bad Sfit* 100  $\mu\text{m}$  flag set to on, the main error comes from the highly biased estimate of the FWHM ( $\sim 31\%$ ), leading to an over-estimate of the fluxes in all bands. This happens when

a strong source is embedded in a faint background (e.g. at high latitude), introducing a degeneracy between the fit of the central elliptical Gaussian and the polynomial fit of the background surface at 100  $\mu\text{m}$ . Although bias and 1- $\sigma$  values are smaller than in the *normal* case due to the strong signal of these sources, we reject this population from the physical analysis, because they could introduce wrong estimates of the physical properties based on a highly biased extension.

If we focus now on the *normal* case, when the photometry algorithm has performed well, we first observe a slight bias of all fluxes estimates. The bias at 100  $\mu\text{m}$  becomes larger when looking into the Galactic plane (11.5% for  $|b| < 25$  compared to 1.4% over the whole sky). The fluxes *Planck* bands, however, are less under-estimated when looking inside the Galactic plane, with biases spanning from 2.5% to 5%. The associated 1 $\sigma$  errors are about 6 to 7% on all-sky and 8-9% in the Galactic plane. The impact of such a biased estimate of the fluxes will be discussed together with the study on the calibration uncertainty in Sect. 4.1. On the other hand, the FWHM estimate are typically biased by less than 1% and have an accuracy of  $\sim 18\%$ , when the ellipticity presents no bias and an accuracy of  $\sim 9\%$ . Finally the temperature and spectral index are derived using the method described in Sect. 4.1. Whereas the temperature is slightly underestimated ( $\sim 2\%$  in the Galactic plane), the associated spectral index is over-estimated by  $\sim 7\%$ . The statistical 1- $\sigma$  uncertainties are about 6% and 8% for  $T$  and  $\beta$  respectively. These results will be taken into account in detail when discussing the physical properties of these cold sources in Sect. 4.1.

The Monte-Carlo simulations described here demonstrate the robustness of our photometry algorithm, and justify the rejection of entire categories of objects using the photometry flags, such as the *Aper Forced*, *PS Neg* and *Bad Sfit 100 $\mu\text{m}$* . The re-

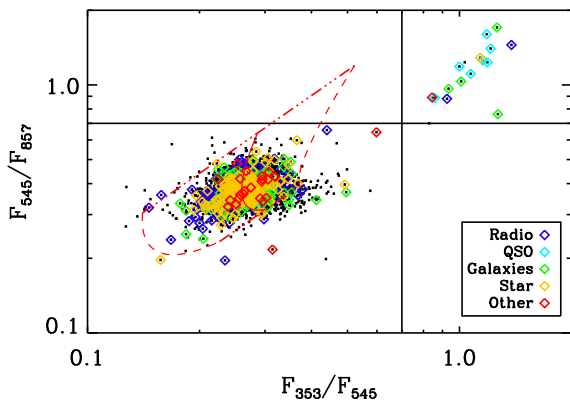


**Fig. 1.** Colour-Colour diagram of the catalogue. The over-plotted symbols stand for the positive cross-matches with non ISM objects. The red contours give the domain of the diagram filled by Archeops cold cores assumed to follow a grey-body law, with a temperature ranging from  $6\text{ K} < T < 25\text{ K}$ , and a spectral index  $\beta$  given by Désert et al. (2008).

maining sample consists of 9465 objects, divided into two categories: 1840 objects have only an upper limit estimate of the flux at  $100\text{ }\mu\text{m}$  and 7625 have well defined photometry in IRAS and *Planck* bands. We will focus on this last category of 7625 sources for the rest of the analysis on the physical properties. Based on this Monte-Carlo analysis, we will adopt the following estimate of the  $1\sigma$  uncertainty on fluxes: 40% on IRAS  $100\text{ }\mu\text{m}$ , and 8% on *Planck* bands. This error is much larger than the intrinsic pixel noise and so instrumental errors are neglected.

### 2.5. Cross-Correlation with existing catalogues

As one step of the validation of our detections, we have performed an astrometric search on the Simbad database<sup>2</sup> for all known sources within a  $5'$  radius of our sources. There are a large number of objects in the Simbad database which raises the question of chance alignments. This is especially true for extragalactic objects which have a reasonably isotropic sky distribution. To judge the number of chance alignments that can be expected by performing this kind of search, we have also conducted a Simbad cross check on the positions of a set of 100 Monte-Carlo simulated catalogues presented in Sect. 5.1.1. These Monte-Carlo realizations reproduce the object density of the *Planck* catalogue per bin of longitude and latitude. The results presented in Table 3 show that the number of coincidences in the *ISM* category is greater in the C3PO catalogue than the probability of chance alignment estimated from the Monte-Carlo simulations. On the contrary, the fraction of contaminants (i.e. *Galaxies*, *QSO*, *Radio Sources*, *stars*) is always lower in C3PO than in the Monte-Carlo realizations. Thus extragalactic objects and Galactic non-dusty objects are mostly rejected by the detection algorithm, whereas actual ISM structures are preferentially detected. A more detailed comparison between C3PO and IRDCs catalogues is presented in Sect. 7.1.

Nevertheless the association with probable contaminants in C3PO is quite high ( $\sim 10\%$ ) and not all are necessarily the result of chance alignments. To disentangle between chance alignment and real matches, we use colour-colour information as shown in Fig. 1. Mostly objects are distributed in the bottom-left corner of the diagram, typical of dust-dominated emitters. The red

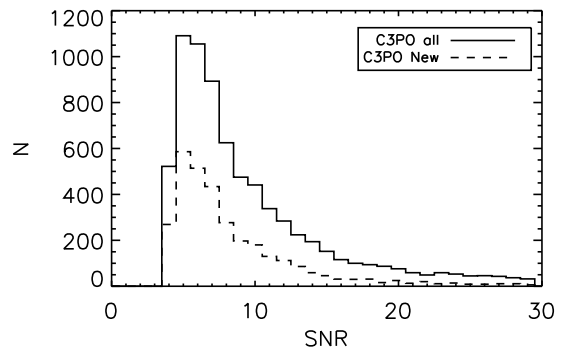


**Fig. 2.** Signal-to-noise ratio (SNR) of new sources (dash line) overlaid on the SNR of all sources (solid line).

Simbad type	C3PO [%]	< MC > [%]
ISM	49.0	21.7
Star	2.3	4.9
Gal	2.1	7.4
Radio	5.3	7.7
QSO	0.1	0.3
Others	0.3	0.2
New detections	40.9	57.8

**Table 3.** Cross match with Simbad database for C3PO and simulated catalogues, for each category of Simbad type. The < MC > column gives an estimate of the probability of chance alignment for each Simbad type.

contours of this figure show the domain filled by dusty objects assuming a grey-body emission law, with  $6\text{ K} < T < 25\text{ K}$ , and a spectral index  $\beta$  given by Désert et al. (2008). The match between *Planck* detections and this colour-colour domain is strong. Only a few objects (17) show the colour-colour properties of radio emitters, located in the top-right corner, indicating real matches with extragalactic objects. For the rest of the sample, the probability of chance alignment is high. Concerning the association with *stars*, except for a few X-ray emitters, mostly all Simbad matches seem associated with dusty emission, and thus represent chance alignment.

We finally reject only the obvious extragalactic matches, located in the top-right corner of the colour-colour diagram, leading to 7608 objects.

Out of the 7608 sources in the photometric reliable catalogue, 40 % have no counterpart in the Simbad database. In addition, these *new* detections have a similar SNR distribution as the entire catalogue as shown in Fig. 2, and can be considered as reliable as the entire catalogue.

## 3. Spatial Distribution

### 3.1. Association with Galactic structures

The all-sky distribution of the 10783 C3PO sources is presented in the upper panel of Fig. 3. Mostly concentrated in the Galactic plane, the distribution clearly follows Galactic structures between latitudes of  $-20^\circ$  and  $+20^\circ$ . A few detections are observed at high Galactic latitude ( $|b| > 30^\circ$ ) and after cross-correlation with external catalogues have been confirmed not to be extragalactic objects (see Sect. 2.5).

<sup>2</sup> <http://simbad.u-strasbg.fr/simbad/>



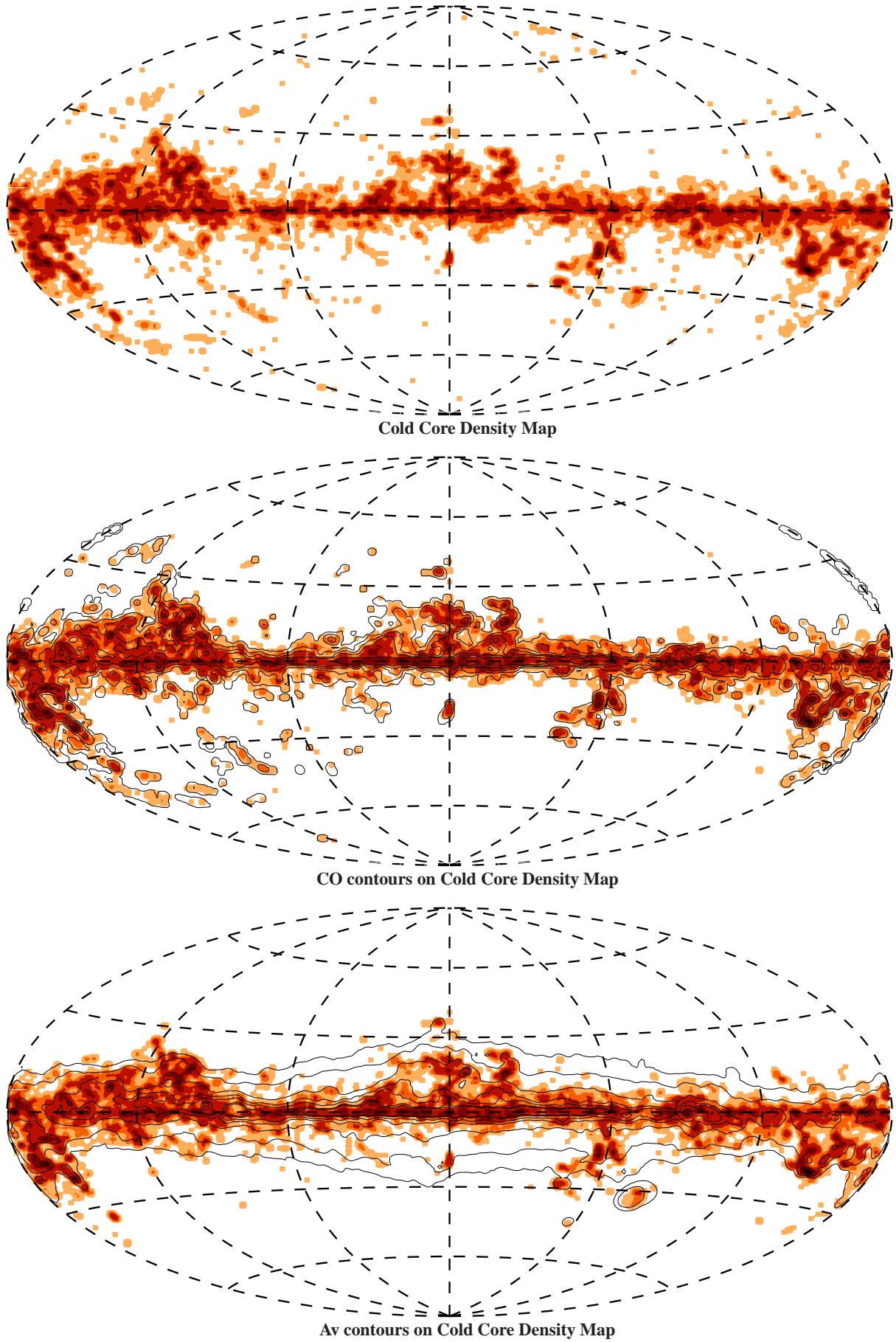


**Fig. 3.** Upper panel: All-sky map of the number of C3PO *Planck* cold clumps per sky area, smoothed at  $3^\circ$ . Middle panel: CO contours are over-plotted on the C3PO density map which is set to 0 where CO map is not defined. Lower panel:  $A_V$  contours are over-plotted on the C3PO density map which is set to 0 where  $A_V$  map is lower than 0.1  $A_V$ .

In the middle panel of Fig. 3, contours of the integrated intensity map of the CO J1-0 line are overlaid on the *Planck* cold clumps density all-sky map. This CO map is a combination of CO data from Dame et al. (2001) and NANTEN data (Fukui et al. 1999; Matsunaga et al. 2001; Mizuno & Fukui 2004), as defined in Planck Collaboration (2011b). The correlation between CO and C3PO Cold Clumps is quite impressive and demonstrates once again the robustness of the detection process and the consistency of the physical nature of these *Planck* cold objects. A detailed analysis shows that more than 95% of the clumps are associated with CO structures.

The lower panel shows the same kind of spatial correlation with the all-sky Av map (Dobashi 2011 in preparation). The Av map traces more diffuse regions of the Galaxy and extends to higher latitude, where cold clumps are also present. About 75% of the C3PO objects are associated with an Av signature greater than 1.

### 3.2. Distance Estimation

Distance estimates are essential to properly analyse the population of detected cold clumps. We have used four different methods: association with IRDCs, association with known molecular complexes, three dimensional extinction method using 2MASS data, and extinction method using SDSS data.

#### 3.2.1. Distances to IRDCs

Simon et al. (2006b) and Jackson et al. (2008) provide kinematic distance estimates for a total of 497 IRDCs extracted from the MSX catalogue (Simon et al. 2006a) that consists of 10931 objects. Kinematic distances are obtained via the observed radial velocity of gas tracers in the plane of the Galaxy. By assuming that the Galactic gas follows circular orbits and a Galactic rotation curve, an observed radial velocity at a given longitude corresponds to a unique Galactocentric radius. Of course, this means that in the inner Galaxy, two heliocentric distances are possible. This technique is only applicable in the plane and requires the availability of appropriate molecular data. We find 127 *Planck* cold clumps, over the complete catalogue, associated with IRDCs that already have a kinematic distance estimate. This number decreases to 32 associations over the 7608 objects of the *photometric reliable* C3PO catalogue.

A more recent work by Marshall et al. (2009) uses an extinction method, detailed in Sect. 3.2.3, on the same MSX catalogue of IRDCs to derive the distance of 1259 objects. This yields 188 associations with C3PO clumps over the entire catalogue, and 47 over the *photometric reliable* C3PO catalogue.

#### 3.2.2. Distances to known molecular complexes

The all-sky distribution of cold clumps follows known molecular complexes. Many of these have distances estimates in the literature. To assign the distance of a complex to a particular cold clump we use the CO map of Dame et al. (2001) to trace the structure of the molecular cloud above a given threshold, and test for the presence of cold clumps inside this region. The association has been performed on 14 molecular complexes (see Table 4), leading to 1152 distance estimates over the entire catalogue and 947 on the photometrically reliable catalogue.

Name	Lon [deg]	Lat [deg]	Area [deg <sup>2</sup> ]	Distance [pc]	Nb
Aquila Serpens	3	28	30	260	59
Polaris Flare	24	123	134	150	55
Camelopardalis	20	148	159	240	11
Ursa Major	35	148	44	240	13
Taurus	-15	170	883	140	393
Taurus Perseus	-15	170	883	350	227
$\lambda$ Ori	-13	196	113	400	66
Orion	-9	212	443	450	353
Chamaeleon	-16	300	27	150	114
Ophiuchus	17	355	422	150	311
Hercules	9	45	35	300	16

**Table 4.** Molecular complexes used to associate C3PO cold clumps to Galactic well-known structures, for which an estimate of the distance is available.

#### 3.2.3. Distances from extinction signature

Genetic forward modelling (using the PIKAIA code Charbonneau 1995) is used along with the Two Micron All Sky Survey (Skrutskie et al. 2006) and the Besançon Galactic model (Robin et al. 2003) to deduce the three dimensional distribution of interstellar extinction towards the cold clump detections. The derived dust distribution can then be used to determine the distance and mass of the sources, independently of kinematic models of the Milky Way. Along a line of sight that crosses a cold clump, the extinction is seen to rise sharply at the distance of the cloud. The method is fully explained in Marshall et al. (2006) and Marshall et al. (2009).

The distance, as determined by this technique, provides line of sight information on the dust distribution. However, it does not have sufficient angular resolution to perform morphological matches on the cold clumps. To ensure that the extinction rise detected along the line of sight is indeed related to the inner structure we perform a consistency check on the column density derived from the extinction and from the source flux, corrected for its temperature. Only detections where the two column densities are in agreement within a factor of two are retained. This leads to distance estimates for 978 objects of the entire and *photometric reliable* catalogue.

#### 3.2.4. Distances from SDSS

Distances to cold clumps within 1 kpc are obtained by analysis of distance-reddening relations for late spectral type stars within the line of sight to each source (Mc Gehee 2011 in preparation). Specifically, we use Sloan Digital Sky Survey photometry of M1 to M5 dwarfs colour-selected by the reddening-invariant index

$$Q_{gri} = (g - r) - \frac{E(g - r)}{E r - i} (r - i). \quad (2)$$

The updated *ugriz* reddening coefficients of Schlafly et al. (2010) are used. The median stellar locus of Covey et al. (2007) forms the basis of a calibration between  $Q_{gri}$  and the intrinsic  $g - i$  colour. After dereddening, the distance to each star is determined including corrections for Galactic metallicity variation following Bochanski et al. (2010).

The distance-reddening profile is constructed by computing the median reddening for stars within a circular patch centered on the core location for 25 pc wide distance bins spanning 0 to 2000 pc. We fit the observed reddening profile to the model



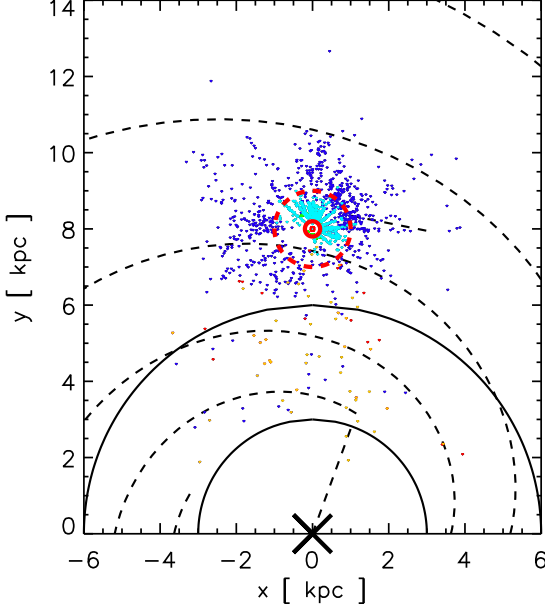


**Fig. 4.** Distribution of C3PO cold clumps as seen from the North Galactic Pole. Colours stand for methods used to estimate distance: Molecular Complex association (green), SDSS extinction (light blue), 2MASS extinction (dark blue), IRDCs extinction (orange) and IRDCs kinematic (red). The red dashed circle shows the 1 kpc radius around the sun. Black dashed lines represent the spiral arms and local bar. The black circles give the limits of the molecular ring.

defined by convolution of the near-field plus single cloud profile with a Gaussian (in distance modulus), this function is:

$$E(B - V)_{obs} = a + c \int_{-\infty}^{x-x_0} \frac{1}{\sqrt{2\pi\sigma^2}} \exp\left(\frac{-t^2}{2\sigma^2}\right) dt \quad (3)$$

where  $x$  is the independent variable (distance modulus),  $x_0$  is the location of the single cloud,  $a$  is the near-field reddening,  $c$  is the reddening associated with the cloud, and  $\sigma$  is the width of the Gaussian. The fitted  $\sigma$  values are typically 0.4 to 0.5 magnitudes in  $m - M$ , as expected from the standard deviation of the  $(r - z, M_r)$  used to assign absolute magnitudes.

Analysis of calibration fields containing well-studied molecular cloud complexes, e.g. the Orion B Cloud, reveal that the recovered distance moduli are underestimated by 0.2 to 0.3 magnitudes, consistent with the bias expected from the M dwarf multiplicity fraction.

This processing leads to 1452 distance estimates over the entire catalogue and 1004 over the *photometric reliable* one.

### 3.2.5. Combined results

The number of sources for which distances could be recovered depends on the method used (cf Table 5). There is some overlap but each method has its distinct advantages according to the distance range being considered. The 2MASS extinction method is not very sensitive nearby ( $D < 1$  kpc), as there are not enough stars to determine accurately the line of sight information. In contrast, the extinction method using SDSS is especially designed for nearby objects. For objects with 1 kpc, we have used SDSS distances when available or molecular complex distances.

Method	Entire C3PO (10783)	Reduced C3PO (7608)
IRDCs (Kinematic)	127	32
IRDCs (Extinction)	188	47
2MASS Extinction	978	978
SDSS Extinction	1452	1004
Molecular Complexes	1152	947
Total	3411	2619

**Table 5.** Number of distance estimates available of the C3PO sources for each method. Notice that the total numbers are not equal to the sum of all methods, due to overlap between them.

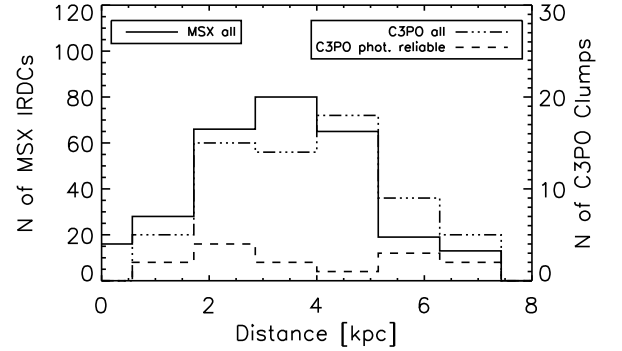


**Fig. 5.** Distance distribution of the MSX IRDCs (Simon et al. 2006b) (solid line) and of the subset associated to the cold clumps of the entire C3PO catalogue (dot-dash-dash line) and the *photometric reliable* subset of C3PO (dotted line).

The number of objects for which we have a distance estimate is 2619 out of a total of 7608 objects in our *photometric reliable* subset, i.e.  $\sim 34\%$ . The distances of the cold clumps span from 0.1 to 7 kpc, but they mainly concentrated in the nearby Solar neighbourhood as shown on Fig. 4. This type of distribution has been already demonstrated using simulations, see Fig. 10 of Montier et al. (2010). The lack of detections at large distances is mainly caused by the effects of confusion within the Galactic plane, from which suffers the detection method. Nevertheless, when comparing the distance distribution of the C3PO cold clumps associated to MSX IRDCs with the total sample of Simon et al. (2006b) in Fig. 5, we notice that the fraction of C3PO - IRDCs matches does not depend on distance and extends to 8 kpc.

Because the subset of C3PO cold clumps with a distance estimate has been obtained using different methods, exploring various regions and distances over the sky, this sample appears heterogeneous. The completeness of the catalogue with distances is quite difficult to assess. Thus we define two subsets for further analysis, especially when looking at number counts, for which we know that the sample is more homogeneous: the first subset (1790 objects) deals with the local objects ( $D < 1$  kpc) and uses only estimates from molecular complexes association and SDSS extinction; the second subset (674 objects) focuses on distant objects ( $D > 1$  kpc) and uses only 2MASS extinction estimates and IRDCs associations.

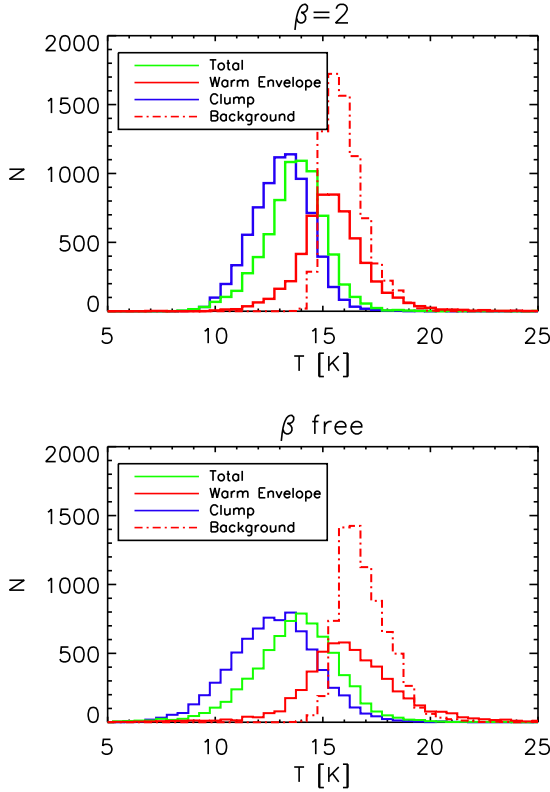


**Fig. 6.** Distribution of the temperature of the cold clumps (blue), of the warm envelope (red) and of the total (green) estimated inside the elliptical Gaussian of the clump itself. The averaged temperature of the local background is plotted in red dot-dash line.

## 4. Physical Properties

### 4.1. Temperature

The temperature of the sources is estimated from SEDs using 4 bands: the IRAS 100  $\mu\text{m}$  and the three highest frequency *Planck* bands 857 GHz, 545 GHz and 353 GHz. The assumed emission model is a modified black-body law, defined as:

$$S_\nu = AB_\nu(T)\nu^\beta, \quad (4)$$

where  $S_\nu$  is the flux integrated over the solid angle  $\Omega_C = \pi\sigma_{\text{Maj}}\sigma_{\text{Min}}$ ,  $A$  is the amplitude,  $T$  is the temperature,  $\beta$  is the spectral index and  $B_\nu$  is the Planck function.

For each source, a set of four temperatures is measured: (1) the temperature of the clump  $T_C$  is defined as the temperature based on the SEDs of the *cold residual* as described in Sect. 2.3; (2) the temperature of the warm envelope  $T_{\text{env}}$  is obtained from aperture photometry over the same region but performed on the *warm component*; (3) the total temperature  $T_{\text{tot}}$  is defined as the temperature of the source in the initial map, i.e. without removing any warm component; (4) the temperature of the local background  $T_{\text{bkg}}$  is defined as the temperature of the average surface brightness around the source.

We have first fixed the spectral index to  $\beta = 2$  (Boulanger et al. 1996). A  $\chi^2$  fit is performed on the SEDs to derive all estimates of temperatures and associated 1- $\sigma$  errors. The distribution of these temperatures is shown on the upper panel of Fig. 6. The temperature of the cores  $T_C$  (blue line) peaks at 13.4 K and spans from 9 K to 16 K. The temperature of the total  $T_{\text{tot}}$  (green

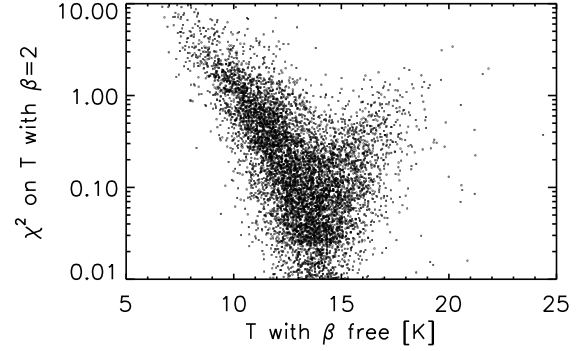


**Fig. 7.** Reduced  $\chi^2$  obtained in the case  $\beta = 2$  as a function of the temperature obtained with  $\beta$  free. When  $T$  becomes lower, the  $\chi^2$  becomes larger.

line), of the warm envelope  $T_{\text{env}}$  (red line), and of the local background  $T_{\text{bkg}}$  (red dot dash line) distributions peak respectively at 13.9 K, 15.1 K and 16.1 K. The uncertainty on the temperature estimates is about 7%. These results are in good agreement with the expected values of cold cores (e.g. [Bergin & Tafalla 2007](#)) and consistent with the results of our Monte-Carlo simulations demonstrating that our source extraction method accurately recovers the cold source parameters in the presence of a warmer background.

In a second analysis, we performed a three parameter ( $A$ ,  $T$  and  $\beta$ )  $\chi^2$  fit leading to the temperature distributions shown in the lower panel of Fig. 6. The  $\chi^2$  fit is performed on a grid taking into account the colour correction as defined in [Planck HFI Core Team \(2011b\)](#) and gives the exact minimum of the  $\chi^2$  in the ( $A$ ,  $T$ ,  $\beta$ ) space and providing the associated 1- $\sigma$  uncertainty. Evaluating the  $\chi^2$  obtained with  $\beta = 2$  as a function of the best fit temperature obtained from the full three parameter fits, we see that a model  $\beta = 2$  is reasonable for temperatures in the range  $10 \text{ K} < T < 18 \text{ K}$  (for which the  $\chi^2 < 1$ ), but does not provide a good fit at lower temperature  $T < 10 \text{ K}$  (see Fig. 7). In fact, the lower the temperature, the worse the fit. Using  $\beta$  as a free parameter, the temperature distributions peak at 13 K, 13.9 K, 15.5 K and 17 K for  $T_C$ ,  $T_{\text{tot}}$ ,  $T_{\text{env}}$  and  $T_{\text{bkg}}$  respectively, with an error of about 7%. The associated spectral index  $\beta$  varies from 1.5 to 3, with an uncertainty of 21% and a mean value of 2.1 for cold clumps and 1.8 for the total emission, consistent with other studies based on *Planck* data ([Planck Collaboration 2011o,t,u](#)). The temperature of the cold clumps span the range 7 K to 17 K.

The bias and the uncertainty of the temperature and spectral index have to be adjusted, taking into account the Monte-Carlo analysis of the photometry algorithm (see Sect. 2.4), and the impact of the calibration uncertainty detailed in Sect. B. We recall that a bias of  $\sim -2\%$  on  $T$  and  $\sim 7\%$  on  $\beta$  is induced by the photometry itself. On the other hand, the calibration uncertainty of fluxes does not introduced any bias on  $T$  or  $\beta$ , but generates an error of  $\sim 8\%$  on  $\beta$  and from 3% to 5% on  $T$ , that should be added quadratically to the uncertainty due to statistical errors. All these considerations lead to a final range of temperature spanning the range 7 K to 17 K with an uncertainty of about 9%, and a spectral index  $\beta$  varying from 1.4 to 2.8 with an uncertainty of about 23%.

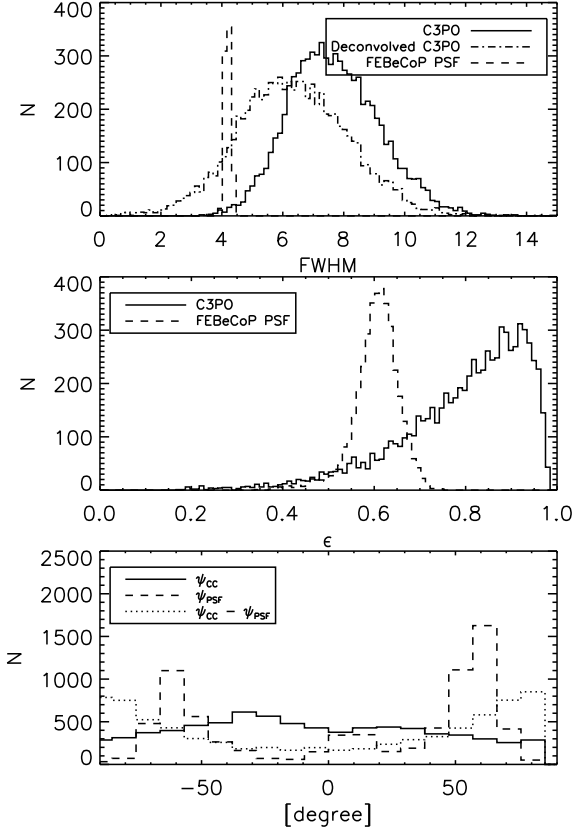


**Fig. 8.** Upper panel: distribution of the FWHM of the *Planck* detections compared to the distribution of the local PSF at 857 GHz (dashed line). Middle panel: distribution of the ellipticity of the cold clumps (solid line) and of the local PSF (dashed line). Lower panel: distribution of the position angle of the elliptical Gaussian of the clumps (solid line), of the local PSF (dashed line), and difference between both (dotted line).

#### 4.2. Extension and ellipticity

The extension and ellipticity of the sources derived during step 1 of the photometry algorithm described in Sect. 2.3 have been compared with the local Point Spread Function (hereafter PSF) provided by the FElBeCoP tool (Mitra et al. 2010) at 857 GHz. This PSF takes into account the scanning strategy and the pixelization of the maps at each location of the sky. Thus for each source, an elliptical Gaussian fit is applied on the PSF smoothed at  $4.5''$  to get the local FWHM  $\theta_{\text{PSF}}$ , ellipticity  $\epsilon_{\text{PSF}}$  and position angle  $\psi_{\text{PSF}}$  of the effective beam. The FWHM  $\theta$  is defined as the geometric mean of the major and minor axis widths:

$$\theta = \sqrt{(\theta_{\text{Maj}} \cdot \theta_{\text{Min}})}, \quad (5)$$

and the ellipticity is given by:

$$\epsilon = \sqrt{1 - \left(\frac{\theta_{\text{Min}}}{\theta_{\text{Maj}}}\right)^2}. \quad (6)$$

A few examples of FElBeCoP beams for *Planck* HFI detectors are given in Fig. B.5 of Planck Collaboration (2011r). Fig. 8 compares the statistical distributions of the FWHM (upper panel), ellipticity (middle) and position angle (lower panel) between C3PO sources (solid line) and the local PSF at 857 GHz (dashed line).

Cold clumps are clearly extended, with an average value of  $\theta_C$  of  $7.7''$  compared to the  $4.3''$  of the average PSF over the sky. Assuming that these compact sources are resolved by the *Planck* beam, we can deconvolve them to derive the inferred intrinsic source size  $\theta_i$  (dot-dash line in Fig. 8):

$$\theta_i = \sqrt{\theta_C^2 - \theta_{\text{PSF}}^2}, \quad (7)$$

where  $\theta_C$  is the extension of the source and  $\theta_{\text{PSF}}$  is the PSF extension. We find that  $\theta_i/\theta_{\text{PSF}} \approx 1.4$ , and could conclude that we have resolved the sources. Nevertheless, as pointed out by Enoch et al. (2007) and Netterfield et al. (2009), the fact that the cold sources are mostly extended compared to the PSF is an indicator of the hierarchical structure of these objects. Netterfield et al. (2009) show that the BLAST sources present the same behavior with a ratio between the inferred source size and the BLAST beam equal to 1.1. Enoch et al. (2007) obtained a value of 1.5 for cold cores in Serpens, Perseus and Ophiucus observed with Bolocam. Indeed these compact sources are associated to larger envelopes presenting radial density profiles in power law with an exponent equal to -2 to -1 (Young et al. 2003).

Cold clumps are also mostly elongated, with a distribution of axial ratios extending to values as large as 5 and peaking at around 1.5, compared to the mean value of 1.3 for the local PSF. Note that the C3PO cold clumps are not preferentially aligned with the major axis of the PSF, the position angles of the elliptical clumps and of the PSF are uncorrelated. As also stressed by Planck Collaboration (2011r), cold cores are often associated with filaments and parts of larger elongated cold structures where star formation occurs. This was noted a long time ago by Barnard (1907) for Taurus, and it has more recently been investigated by Herschel observations in Polaris (Men'shchikov et al. 2010) and Aquila (Könyves et al. 2010). This characteristic of the cold core population can now be addressed more generally using the *Planck* all-sky data and is discussed in detail in Sect. 5.

When distances are available (see Sect. 3.2), we can derive the physical size of the sources, defined as the FWHM in pc. Fig. 9 presents the statistical distribution of the size obtained for 2619 sources. A distinction is made between local ( $D < 1\text{ kpc}$ , dashed line) and distant ( $D > 1\text{ kpc}$ , dot-dash line) sources as defined in Sect. 3.2.5. The relation of Elmegreen & Falgarone (1996) and Heyer et al. (2001), a size spectral index of -2.3 typical of dust clouds, is over-plotted on the distributions of the two subsets.

#### 4.3. Column Densities

The column density values averaged over the clump solid angle can be derived from the integrated flux using :

$$N_{\text{H}_2} = \frac{S_{\nu_0}}{\Omega_C \mu m_{\text{H}} \kappa_{\nu_0} \times B_{\nu_0}(T)}, \quad (8)$$

where  $\Omega_C = \pi \sigma_{\text{Maj}} \sigma_{\text{Min}}$  is the solid angle,  $\mu = 2.33$  is the mean molecular weight,  $m_{\text{H}}$  is the mass of atomic hydrogen,  $\kappa_{\nu_0}$  is the dust opacity (or mass absorption coefficient), and  $B_{\nu_0}(T)$  is the Planck function for dust temperature at  $T$ . We compute two different column densities, one for the core  $N_{\text{H}_2}^{\text{C}}$  (with  $T_{\text{C}}$  and  $S_{\nu_0}^{\text{C}}$ ) and the second for the total integrated flux along the line of sight  $N_{\text{H}_2}^{\text{full}}$  (with  $T_{\text{full}}$  and  $S_{\nu_0}^{\text{full}}$ ) to give an indication of the density of the surrounding environment. The main source of uncertainty here comes from the value adopted for  $\kappa_{\nu}$ . Large variations arise from one dust model to another, depending on the dust properties considered : composition (with or without ice mantles),



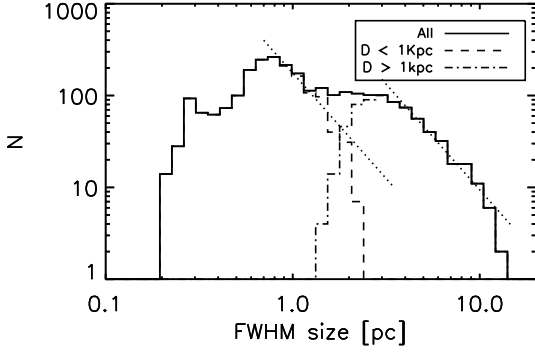


**Fig. 9.** Distribution of the physical size of the cold clumps in pc. The distinction is done between the local sample ( $D < 1\text{ kpc}$ , dashed line) and the distant sample ( $D > 1\text{ kpc}$ , dot-dash line). A power law with  $\alpha = -2.3$  is overlaid in dotted line over the 2 subsets.

structure (compact or fluffy aggregates), size... (see reviews from Beckwith et al. 1990; Henning et al. 1995). Dust models and observations show that  $\kappa_\nu$  values can vary by a factor of 3-4 (or higher) from diffuse to dense and cold regions (Ossenkopf & Henning 1994; Kruegel & Siebenmorgen 1994; Stepnik et al. 2003; Juvela et al. 2010).

For this study, we have adopted the dust opacity from Beckwith et al. (1990) in agreement with the recommendation for dense clouds at intermediate densities ( $n_{\text{H}_2} \leq 10^5$ ) (Preibisch et al. 1993; Henning et al. 1995; Motte et al. 1998):

$$\kappa_\nu = 0.1(\nu/1000\text{GHz})^\beta \text{ cm}^2\text{g}^{-1}, \quad (9)$$

where we take a standard emissivity spectral index  $\beta = 2$ . As  $\nu_0$  is set to 857 GHz that is close to the 1000 GHz of the formula, the impact of variability of the spectral index  $\beta$  remains small compared to the uncertainty of  $\kappa_\nu$ . For  $\beta$  varying from 1 to 3,  $\kappa_{\nu_0}$  varies of a maximum of 15% around the value obtained with  $\beta = 2$ .

For the clumps for which the distance could be estimated, we have also determined an approximate averaged volume density value with :

$$n_{\text{H}_2}^C = N_{\text{H}_2}^C / \sigma_{\text{Min}}, \quad (10)$$

where the third size dimension of the object is taken as equal to the minimum value of the clump 2D size  $\sigma_{\text{Min}}$ .

Fig. 10 shows the column densities  $N_{\text{H}_2}^{\text{full}}$  (lower panel) and  $N_{\text{H}_2}^C$  (upper panel). The column density associated with the inner clump are systematically higher than the full column density, because it is tracing the colder and denser phase of the medium. We also compare the observed column density of the clump with Bonnor-Ebert models of cold cores (Bonnor 1956; Ebert 1955; Fischera & Dopita 2008) placed at 200 pc and for masses spanning from  $0.2 M_\odot$  (blue) to  $12 M_\odot$  (red): The triangles correspond to a normal radiation field (Mathis et al. 1983) around the cold core, while the diamond correspond to the case of a radiation field already attenuated by external dust with  $A_V=2$ . This modeling does not match well with the observations. One explanation is first that the Bonnor Ebert sphere modeling is only valid until  $M = 20 M_\odot$  as stressed in Montier et al. (2010), whereas the mass range of the C3PO catalogue is much larger as detailed in Sect. 4.4. Moreover it does not take into account the dilution inside the beam. This comparison shows also that the *Planck*

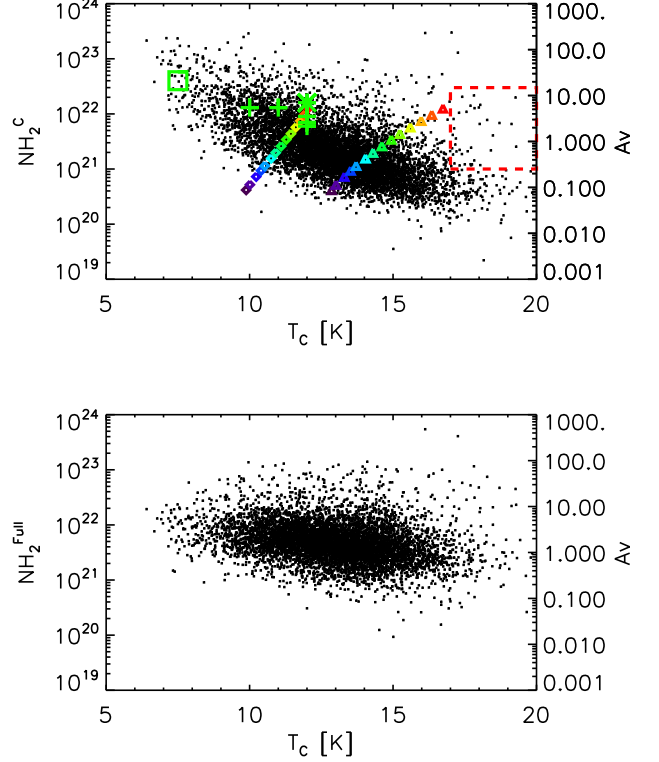


**Fig. 10.** Molecular column density of the clump itself  $N_{\text{H}_2}^C$  (upper panel) and molecular column density of the total line of sight  $N_{\text{H}_2}^{\text{full}}$  (lower panel) as a function of the temperature of the cold clump  $T_c$ . Modeling of Bonnor-Ebert spheres provides the temperature and column densities over-plotted in coloured symbols (triangle and diamond) for mass spanning from 0.4 (blue) to 12 (red) solar masses. The triangles correspond to a normal radiation field (Mathis et al. 1983) around the cold core, when the diamond correspond to the case of a radiation field already attenuated by external dust with  $A_V=2$ . The square, cross and plus green symbols are respectively the very cold core in L134N (Pagani et al. 2004), the Pronaos core in Taurus (Stepnik et al. 2003), and the starless cores of Herschel in Polaris Flare (Ward-Thompson et al. 2010). The dashed red box gives the limits of the domain occupied by the IRDCs of Rathborne et al. (2010).

cold detections cannot be modeled in such a simple way and are probably more complex and extended objects.

We have also over-plotted a few other reference points of starless cores (see caption of Fig. 10). These few objects identified as cold cores are located in the upper distribution of the C3PO catalogue, in the coldest and densest part of the diagram. This underlines again the statistical property of the *Planck* objects that have a mean column density around a few  $10^{21}$  hydrogen atoms per square cm. This can be explained by the *Planck* resolution that preferentially selects quite extended objects, diluting objects smaller than the  $5'$  beam. This will be discussed in detail in Sect. 7.1. Nevertheless, we observe a few objects with column density greater than  $10^{23}$ , even at the *Planck* resolution. These few objects could be precursors of massive stars, or high mass formation regions. Moreover, the locus of the IRDCs studied by Rathborne et al. (2010) is shown as a red dashed box in Fig. 10. This underlies the fact that *Planck* detects clumps having

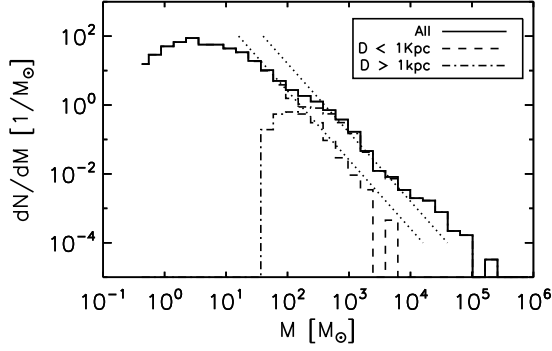


**Fig. 11.** Mass spectrum for total sample (solid line), close sample ( $D < 1$  kpc, dashed line) and far sample ( $D > 1$  kpc, dot-dash line). A power law  $M^{-2}$  (dotted line) is overlaid for both subsets.

the same column density but significantly colder temperatures than the IRDCs.

Finally, we observe that even the densest clumps (with high column densities) cannot reach temperature lower than 7 K. This is in excellent agreement with recent observations of cold cores with Herschel (private communication).

#### 4.4. Mass Distribution

The integrated mass over the clump is defined by:

$$M = \frac{S_{\nu_0} D^2}{\kappa_{\nu_0} B_{\nu_0}(T)}, \quad (11)$$

where  $S_{\nu_0}$  is the integrated flux at the frequency  $\nu_0 = 857$  GHz,  $D$  is the distance,  $\kappa_{\nu_0}$  is the dust opacity (or mass absorption coefficient) as defined in Sect. 4.3, and  $B_{\nu_0}(T)$  is the Planck function for dust temperature at  $T$ . The range of masses of the detected cold clumps spans from  $0.3 M_{\odot}$  up to  $2.5 \times 10^4 M_{\odot}$ , with a median mass of  $88 M_{\odot}$ . The mass spectrum of the cold clumps is estimated by binning the mass distribution into logarithmically spaced bins in mass. The mass spectrum is then calculated from

$$f(M) = \frac{dN}{dM} \approx \frac{N_i}{\Delta M_i}, \quad (12)$$

where  $N_i$  is the number of clouds in bin  $i$  and  $\Delta M_i$  is the width of the  $i^{\text{th}}$  mass bin.

As already stressed in Sect. 3.2.5, it is very difficult to characterize the completeness of the catalogue over the all-sky. The bias induced by the detection method inside the Galactic plane, due to confusion, and induced by the various methods of distance estimate prevents any robust knowledge of the completeness of the sample. Thus the mass spectrum built here is not the mass spectrum of the cold core population of the entire Milky Way. Fig. 11 shows the mass spectrum of the total sample (solid line) and of the two subsets,  $D < 1$  kpc (dashed line) and  $D > 1$  kpc (dot-dash line), as defined in Sect. 3.2.5. A power law,  $dN/dM \propto M^{-\alpha}$  with  $\alpha = 2$  is overlaid (dotted line) on each mass function. We observe that the mass function for local objects is compatible with  $\alpha \sim 2$  over the range  $30 M_{\odot} < M < 2000 M_{\odot}$ , and over the range  $300 M_{\odot} < M < 10^4 M_{\odot}$  for the distant objects. This slope  $\alpha = 2$  is representative of the standard value  $\alpha = 2.1 \pm 0.4$  derived for MSX IRDCs with  $M > 100 M_{\odot}$  by Rathborne et al. (2006). Similar mass function have been obtained on the Pipe Nebula (Alves et al. 2007) (Rathborne et al.

2008), Perseus (Enoch et al. 2006), Ophiuchus (Young et al. 2006), and Serpens (Enoch et al. 2007). They all derive mass function for cold cores in a range of mass  $0.5 M_{\odot} < M < 20 M_{\odot}$  with slopes spanning the range  $\alpha = 1.6$  to  $2.77$  and peaking at around  $\alpha = 2.1$ . An excess of high mass objects is observed for  $M > 10^4 M_{\odot}$ , but the heterogeneity of our sample prevents any further interpretation at this stage of the analysis. A better knowledge of the completeness of the C3PO catalogue and a better consistency between the distance estimates are needed.

#### 4.5. Luminosity

The bolometric luminosity is defined by:

$$L = 4\pi D^2 \int_{\nu} S_{\nu} d\nu, \quad (13)$$

where  $D$  is the distance, and  $S_{\nu}$  is the integrated flux over the clump. The bolometric luminosity,  $L$ , is integrated over the frequency range  $1 \text{ Hz} < \nu < 1 \text{ THz}$ , using the modeled SEDs derived from temperature and spectral index fitting (see Sect. 4.1). The  $L - M$  diagram is shown in Fig. 12. A large majority of the objects is located below the  $L = M$  line (green dot-dash) over the whole range of mass. The loci empirically derived by Molinari et al. (2008) for sources in the accretion stage (light blue) and in the nuclear burning stage (dark blue) are at least two order of magnitude above the domain covered by the C3PO clumps, indicating that accretion and nuclear burning are not dominant in these sources.

The quantity  $L/M$  is very powerful in assessing the evolutionary stage of the sources, and has the advantage that it is independent of distance:

$$\frac{L}{M} = \frac{4\pi \int_{\nu} S_{\nu} d\nu}{\mu m_{\text{H}} \Omega_{\text{C}} N_{\text{H}_2}}, \quad (14)$$

Fig. 13 shows the histogram of  $L/M$  for the high-reliability C3PO catalogue (solid line), for the subset with distances (dashed line), and for all sub-samples corresponding to different methods of distance estimate. Three domains are defined following the formalism of Roy et al. (2010): *Stage E* ( $L/M < 1 L_{\odot}/M_{\odot}$ ) corresponding to the 'Early' stage in which external heating is dominant; *Stage A* ( $1 L_{\odot}/M_{\odot} < L/M < 30 L_{\odot}/M_{\odot}$ ) corresponding to the 'Accretion'-powered stage; and the nuclear burning dominant phase of the star formation ( $L/M > 30 L_{\odot}/M_{\odot}$ ). The C3PO clumps are mainly located in the  $L/M$  domain of Stage E for all sub-samples of the catalogue, indicating that the nature of the objects in the catalogue is homogeneous with distance. Nevertheless about 15% of the C3PO sources have a ratio  $L/M > 1 L_{\odot}/M_{\odot}$  and represent a candidate population of evolved objects in which the accretion process has already started and so could already contain stars. The mean temperature of this population of clumps is around 16 K and spans from 13 K to 18 K, indicating an internal heating due to star formation. For the other 85% of sources that fall into the early stage domain, it is difficult to assess the presence of stars inside the clumps. The lack of angular resolution prevents us from seeing internal sub-structures, so the presence of low-mass YSOs cannot be rejected (as discussed in Roy et al. (2010) for the BLAST population in CygX).

Moreover we have overlaid on the  $L-M$  diagram of Fig. 12 the curves of constant surface density  $\Sigma$  using the theoretical formula of Krumholz (2006):

$$L = 390 \left( \frac{\Sigma}{1 \text{ g cm}^{-2}} \frac{M}{100 M_{\odot}} \right)^{0.67} L_{\odot}, \quad (15)$$

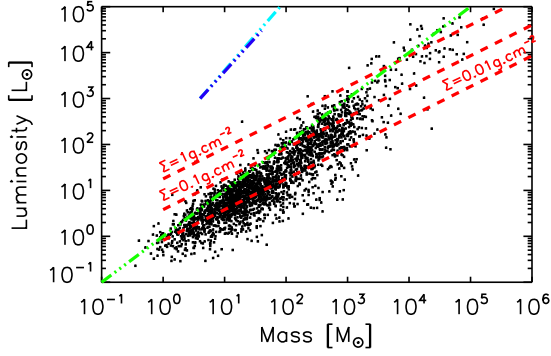


**Fig. 12.** Bolometric luminosity as a function of mass. The  $L = M$  limit is over-plotted in dot-dash green line. The loci of accretion-powered and nuclear burning phases of [Molinari et al. \(2008\)](#) are shown in light and dark blue lines. The theoretical surface densities  $\Sigma$  of [Krumholz \(2006\)](#) are given in dashed red lines for 3 values:  $0.01 \text{ g} \cdot \text{cm}^{-2}$ ,  $0.1 \text{ g} \cdot \text{cm}^{-2}$  and  $1 \text{ g} \cdot \text{cm}^{-2}$ .

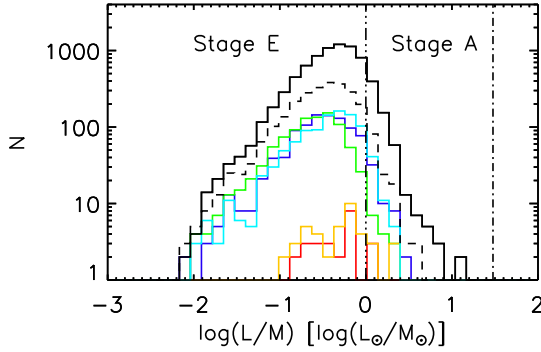


**Fig. 13.** Histogram of the  $L/M$  ratio for the total C3PO catalogue (solid line) and the sub-sample of 2619 objects for which a distance estimate has been obtained (dashed line). The distinction is also done between the various methods used to estimate the distance: Molecular Complex association (green), SDSS extinction (light blue), 2MASS extinction (dark blue), IRDCs extinction (orange) and IRDCs kinematic (red). The vertical lines indicate the theoretical frontiers between the three stages of the star evolution: the early stage 'E', the accretion-powered stage 'A' and the nuclear burning dominant stage.

for 3 values of  $\Sigma=0.01, 0.1$  and  $1 \text{ g cm}^{-2}$  ( $=45, 450$  and  $4500 M_{\odot} \text{ pc}^{-2}$ ). Following recent theoretical work by [Krumholz & McKee \(2008\)](#) suggesting that high-mass stars form from clouds with  $\Sigma > 1 \text{ g cm}^{-2}$ , it appears that only a few *Planck* cold clumps could be considered as precursors of high-mass stars,

## 5. Large and medium scale distribution

The spatial distribution of C3PO clumps is highly nonuniform; they seem to form arcs, groups and filaments (see Fig. 16). These large and small scale distribution anomalies were analysed. We performed an all-sky analysis ( $|b| > 5^{\circ}$ ) and we show results for both all-sky and Tau-Aur-Per-Ori region (hereafter TAPO), where C3PO surface density shows remarkable excess on known large scale loops and shells.

Region		C3PO	MC
TAPO	$N_G$	260	$161 \pm 9$
	$N_{G4}/N_G$	0.17	$0.04 \pm 0.016$
	$\bar{\epsilon}$	2.67	$2.55 \pm 0.920$
All-sky	$N_G$	1833	$988 \pm 25$
	$N_{G4}/N_G$	0.11	$0.06 \pm 0.007$
	$\bar{\epsilon}$	2.64	$2.54 \pm 0.130$

**Table 6.** The number and properties of identified groups in the C3PO data and the Monte Carlo simulations for the TAPO and for the all-sky.  $\bar{\epsilon}$  means the average elongation of the groups.

### 5.1. Medium Scale Structures

#### 5.1.1. Groups

We identified groups in the TAPO region using the Minimum Spanning Tree (MST) method of [Cartwright & Whitworth \(2004\)](#) as described in [Gutermuth et al. \(2009\)](#) and [Beer et al. \(2010\)](#). A cut-off length (i.e. maximum allowed distance between a group member core and a given subgraph) of 16 arcmins was used. It corresponds to the average distance between the nearest neighbours in the C3PO all-sky data. The number of C3PO groups,  $N_G$  in the region is 260. The fraction of groups with more than 3 elements,  $N_{G4}/N_G$  is 17% (see Fig. 14). We identified groups in the all-sky data with the same method. The number of C3PO groups is 1833 and the value of  $N_{G4}/N_G$  is 11%.

In order to assess the reliability of the statistical estimate, we performed a Monte-Carlo analysis consisting in 1000 random realizations. The same number of sources as present in the C3PO catalogue were randomly placed onto the sky, following the (l,b) marginal distributions of the C3PO positions, averaged in latitude and longitude bins of  $5^{\circ}$ .

In the TAPO region in the simulated samples the average number of groups is 161, that is  $\sim 40\%$  less than in the C3PO, see Table 6. There were at maximum 189 groups in the simulated samples, still 30% less than the value for C3PO. The histogram of the number of groups is shown in Fig. 14, where the value for C3PO is marked with a vertical dashed line. The all sky distribution shows similar grouping tendencies. The random samples show in average 988 groups,  $\sim 47\%$  less than in the C3PO. We found at maximum 1083 groups in the simulated samples, still 40% less than the value for C3PO. Our result suggests that the point pattern unlikely has these many groups in random distributions. In the 1000 Monte-Carlo simulated samples the fraction of groups with more than 3 elements is in average 4% in the TAPO region and 6% in the all-sky and is never higher than 11% in the TAPO region and 9% in the all-sky. Their histogram is shown in Fig. 14, where the vertical dashed line marks again the C3PO value. We note that the larger groups are more common in the C3PO than in an average random sample.

We also investigated the variation of  $N_G$  and  $N_{G4}/N_G$  as a function of the cut-off length, that we varied from  $10'$  to  $30'$ . We found that  $N_G$  and  $N_{G4}/N_G$  increase with the cut-off length. For every cut-off length the average  $N_G$  and  $N_{G4}/N_G$  in the simulated data are  $\sim 25\text{--}45\%$  less than in the C3PO data.

#### 5.1.2. Filaments

The elongation of groups was analysed as described in [Schmeja & Klessen \(2006\)](#). We used the [Cartwright & Whitworth \(2004\)](#) definition of cluster radius:  $R^c$  as the distance between the mean



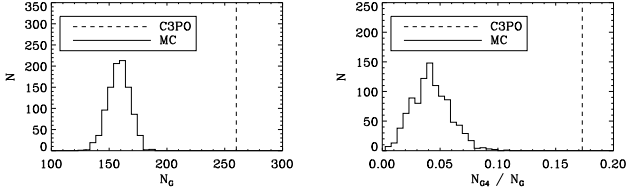


**Fig. 14.** Left: histogram of the number of groups,  $N_G$  in the TAPO region in the Monte-Carlo simulations. Vertical dashed line shows the number of groups identified in the C3PO by using the same method in the same region. Right: histogram of the relative number of groups with 4 or more elements  $N_{G4}/N_G$  for 1000 MC simulations in the TAPO region. Vertical dashed line shows the same value for the C3PO in this region.

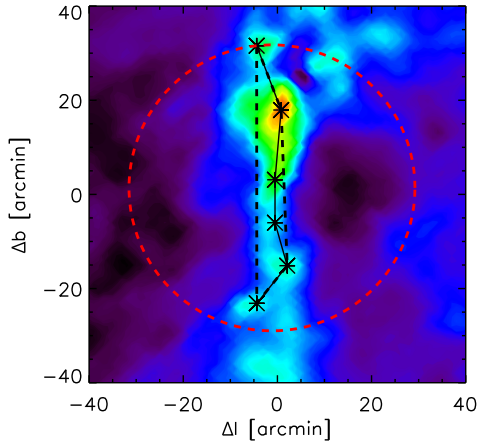


**Fig. 15.** A sample group from the C3PO in the TAPO region. Black asterisks show the clumps, black lines indicate the MST, dark dashed and dotted line indicate the convex hull and the radius of the red dashed circle is ( $R^c$ ).

position of all cluster members and the most distant sources. The area  $A$  of the cluster was estimated using the convex hull (the minimal convex set containing the set of points  $X$  in a real vector space  $V$ ) of the data points. The convex hull radius ( $R^h$ ) is defined as the radius of a circle with an area equal to the  $A$  area of the convex hull of the data points. Cartwright & Whitworth (2004) define the elongation measure  $\xi$  as follows:

$$\xi = \frac{R^c}{R^h}. \quad (16)$$

Fig. 15 shows a sample group from the C3PO in the TAPO region with an elongation measure of  $\xi = 3.4$ .

We calculated the elongation measure for all the 205 larger groups (i.e. with more than 3 members) in the C3PO all-sky data. We found a mean elongation of  $\sim 2.7$  in the TAPO region and  $\sim 2.6$  in the all-sky, see Table 6. The mean elongation of the filaments in the Monte-Carlo simulated samples (see Sect. 5.1.1) does not differ from that in the C3PO in these regions, see Table 6. We note here the very low value of  $N_{G4}$  in the simulated samples. We also investigated the mean elongation in the C3PO data for different cut-off lengths and found that the averaged elongation of the groups is insensitive to the cut-off length and is always around  $\sim 2.6$ ,

Region		C3PO	MC
TAPO	IN	0.764	$0.756 \pm 0.022$
	ON	0.912	$0.853 \pm 0.023$
	OFF	0.792	$1.058 \pm 0.054$
All-sky	IN	0.184	$0.175 \pm 0.002$
	ON	0.322	$0.238 \pm 0.005$
	OFF	0.056	$0.097 \pm 0.002$

**Table 7.** Surface density of C3PO sources and Monte-Carlo simulations for HI supershells in the 3 cases: IN shell, ON shell and OFF areas. Values for both TAPO region and all-sky are presented. For Monte-Carlo simulations, the mean value of the distribution is given with the  $1\text{-}\sigma$  discrepancy.

Region		C3PO	MC
TAPO	IN	0.652	$1.024 \pm 0.033$
	ON	1.212	$0.906 \pm 0.027$
	OFF	0.557	$0.600 \pm 0.023$
All-sky	IN	0.119	$0.135 \pm 0.004$
	ON	0.193	$0.122 \pm 0.003$
	OFF	0.144	$0.173 \pm 0.002$

**Table 8.** Same as Table 7 for IRAS Loops

## 5.2. HI shells and superloops

A first look at the all-sky distribution of the C3PO sources reveals loop-like structures at medium and large scales. Here we quantify this impression and study the associations between these loops and known shells and supershells, already stressed to be locations of star formation. The link between the cold substructures detected by *Planck* and the star formation regions is also discussed within the framework of the triggering scenario (e.g. Deharveng et al. 2005; Zavagno et al. 2010a,b).

### 5.2.1. HI shells

Initially we compared the distribution of C3PO sources and the HI supershells from Heiles (1984). This list of shells contains HI shells, supershells and also shell-like objects and ‘worms’, restricted to shells crossing  $|b| = 10$  or located entirely outside  $|b| = 10$ . These objects were originally derived from two 21 cm line surveys (Weaver & Williams 1973; Heiles & Habing 1974) exhibiting filamentary structure associated with high-velocity gas and radio continuum loops. Heiles (1979) observed that HI shells do not seem to be significantly correlated with any other types of object, except perhaps young stellar clusters.

The comparison of HI shells and C3PO distribution gives the following results: For the TAPO region, 682 (46%) of the clumps are found on the shells, 635 (43%) within them and 153 (11%) outside the shells. For the all-sky sample the corresponding values are as follows: 1869 (33%), 2985 (52%), 873 (15%).

To assess the statistical reliability of these numbers, we performed an equivalent analysis on the 1000 Monte-Carlo simulations introduced in Sect. 5.1.1. The simulated surface density of clumps on the shells is slightly lower ( $3\sigma$ ) than in the real sample, see Table 7.

### 5.2.2. IRAS loops

We also compared the distribution of *Planck* cold clumps to the FIR loops in the IRAS Galactic Infrared Loops of Könyves et al.

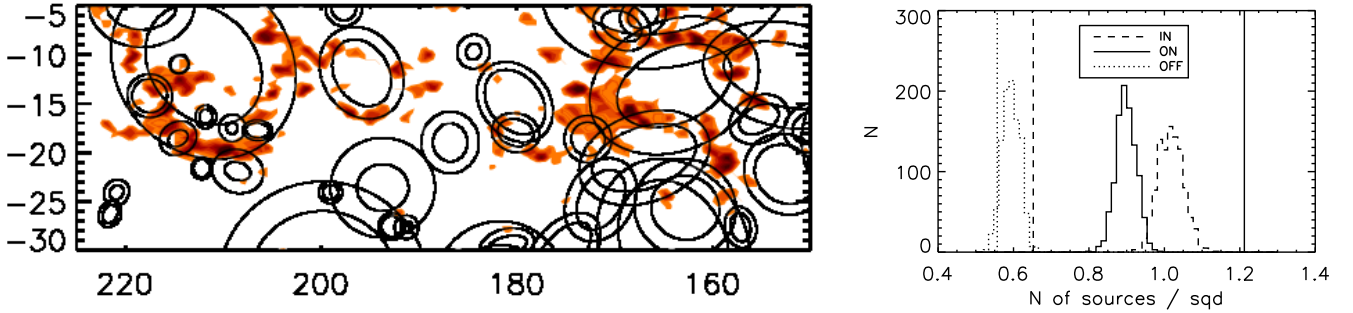


**Fig. 16.** Left: Surface density grayscale map of the C3PO sources with the inner and outer boundaries of FIR loops (Konyves et al. 2006) overlaid. Right: Histogram of the surface density of 1000 Monte-Carlo simulated sources for ON (solid line), IN (dashed line) and OFF (dotted line) areas. Vertical lines show the same for the C3PO clumps, respectively.

(2006). These IRAS loops were identified in an investigation of the large-scale structure of the diffuse interstellar medium (Kiss et al. 2004) based on 60 and 100  $\mu\text{m}$  ISSA plates (IRAS Sky Survey Atlas Wheelock et al. 1994). They have been identified in the Galaxy as surfaces of high and low density ISM (Tóth & Kiss 2007), and have been proposed as locations for star formation (Kiss et al. 2006). These loops by definition must show an excess FIR intensity confined to an arc-like feature extending to at least 60% of a complete ellipse-shaped ring. Dust IR emission maps by Schlegel et al. (1998) were investigated to derive the parameters describing the loop features (Kiss et al. 2004). Comparing the distribution of IRAS loops and the C3PO clumps gives a hint of the correlation between star formation sites and the cold sub-structures of the ISM.

Fig. 16 shows the surface density map of C3PO in TAPO with the FIR loop boundaries overlaid. We found 810 (55%), 312 (21%) and 348 clumps (24%) on the FIR loop shells, inside the loops and in the area between the FIR loops, respectively. Values for the all-sky study are as follows: 1928 (34%), 877 (15%), 2922 (51%). We performed the same analysis as with the Heiles supershells using the Monte-Carlo simulations as described in Sect. 5.1.1, see Table 8. We present the histogram of surface density distribution of the Monte-Carlo realizations for the IN, ON and OFF (between loops) areas in Fig. 16b. The vertical lines give the C3PO observations. A significant ( $> 30\%$ ) excess of C3PO clumps on the FIR loop shells in the TAPO region is found in compared to the simulations. The same behaviour is observed on the all-sky analysis (see Table 8).

This analysis shows that the all-sky distribution of the C3PO cold clumps shows a significant correlation with known large scale loops, identified to be star formation regions. It is even more reliable in the case of IRAS loops for which this correlation is detected at  $23\sigma$  compared to Monte-Carlo simulations. It is detected at  $15\sigma$  for HI supershells on the all-sky data, but only at  $2.6\sigma$  in the TAPO region.

### 5.3. Triggering

In this subsection, we explore, from a qualitative point of view, correlations between the spatial location of *Planck* cold clumps and that of candidate sources of star formation triggering. A sig-

nificant body of evidence (e.g. Deharveng et al. 2005; Zavagno et al. 2010a,b) has recently been found to support the so-called *collect and collapse* scenario, in which the swept up shell generated by the radiation pressure associated with newly born stars is the preferential location for the formation of a second generation of stars. Alternatively, triggered star formation may occur within the swept up shell itself, as discussed by Elmegreen (1998).

In this study we consider, in addition to the *Planck* cold clumps, three classes of objects, namely: the 13 most luminous sources recently identified by Murray & Rahman (2010) in the WMAP (Wilkinson Microwave Anisotropy Probe, Bennett et al. 2003) free-free map and thought to be responsible for the bulk of the ionizing luminosity of the Galaxy; the 41 very massive star formation complexes (SFCs) found by Rahman & Murray (2010) to be associated with the WMAP sources; the catalogue of bubbles by Churchwell et al. (2006), the majority of which are thought to be signposts of HII regions. The ensemble of these three classes of objects might be representative, on different angular scales, of different stages of a triggering scenario, with the WMAP sources being the *super-giant* bubbles (scale of multiple supermassive star formation complexes), the Rahman & Murray’s SFCs acting as the *super* bubbles (scale of a supermassive star formation complex), and the Churchwell et al.’s sources representing the *common* bubbles (scale of a typical OB association). Given the preliminary nature of the analysis here described, and due to the relatively low *Planck* angular resolution, we do not take into account smaller star formation complexes, such as compact and ultra-compact HII regions.

The 13 WMAP sources are all located along the Galactic Plane. As for the SFCs of Rahman & Murray (2010) and the bubbles in the catalogue by Churchwell et al. (2006), these have been mostly identified using the data from the Spitzer GLIMPSE (Galactic Legacy Infrared Mid-Plane Survey Extraordinaire Benjamin et al. 2003) survey, which only covers the inner Galactic Plane (first and fourth quadrant). Taking into account the size of the WMAP sources and the coverage of the GLIMPSE survey, we restrict our analysis to the longitude range  $10^\circ < l < 65^\circ$  and  $295^\circ < l < 350^\circ$ ,  $|b| < 2^\circ$ . Despite the limited area, this is where the bulk of the Galactic star formation takes place. At the same time, it is important to bear in mind that

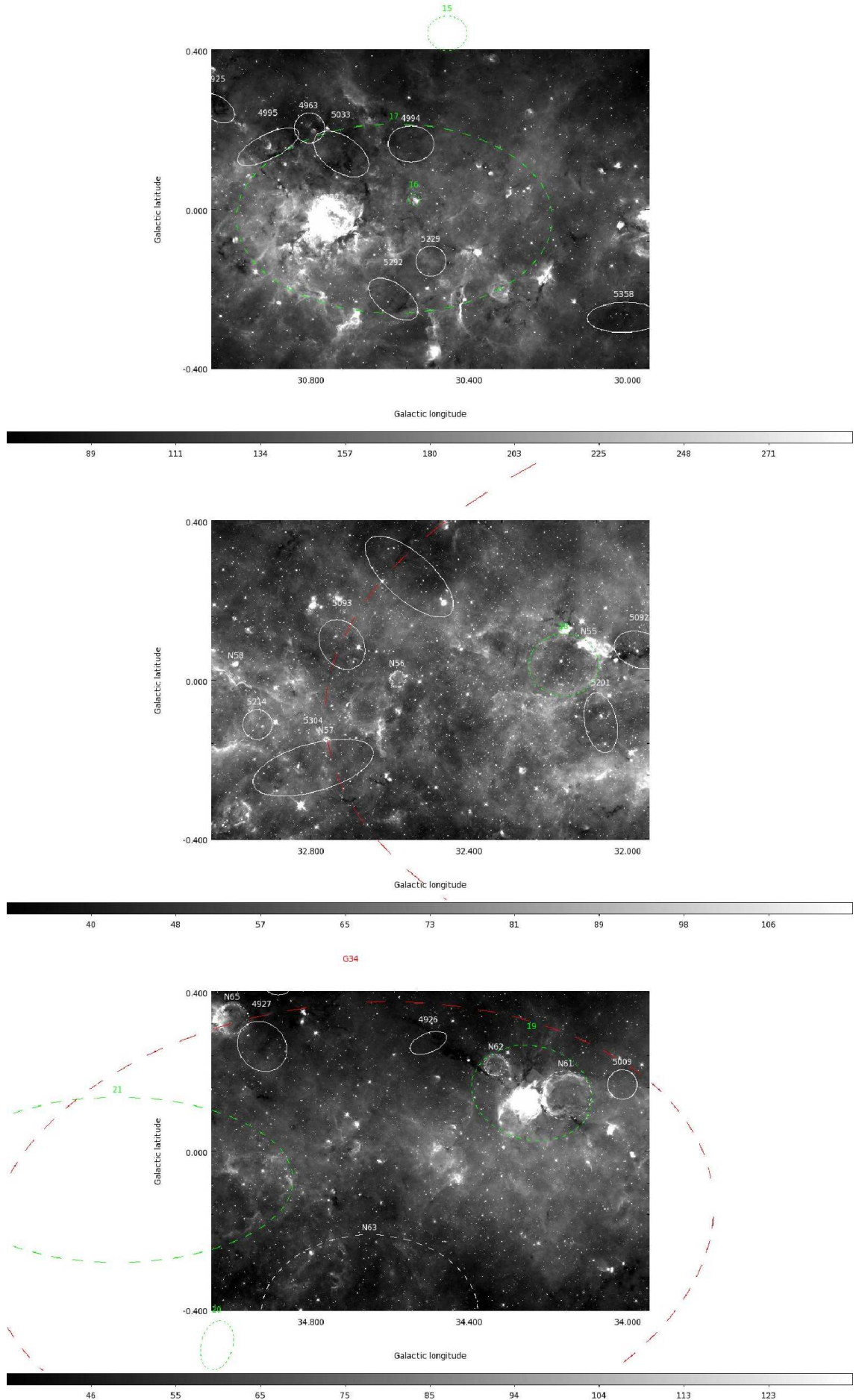


**Fig. 17.** Spatial location of: *Planck* clumps (white solid line), Churchwell's bubbles (white dashed line), SFCs from [Rahman & Murray \(2010\)](#) (green dashed line), WMAP sources from [Murray & Rahman \(2010\)](#), red dashed line). Plain numbers correspond to entries in the C3PO catalogue, while N are names of bubbles in Churchwell's compilation. Background data are from GLIMPSE  $8\mu\text{m}$ .



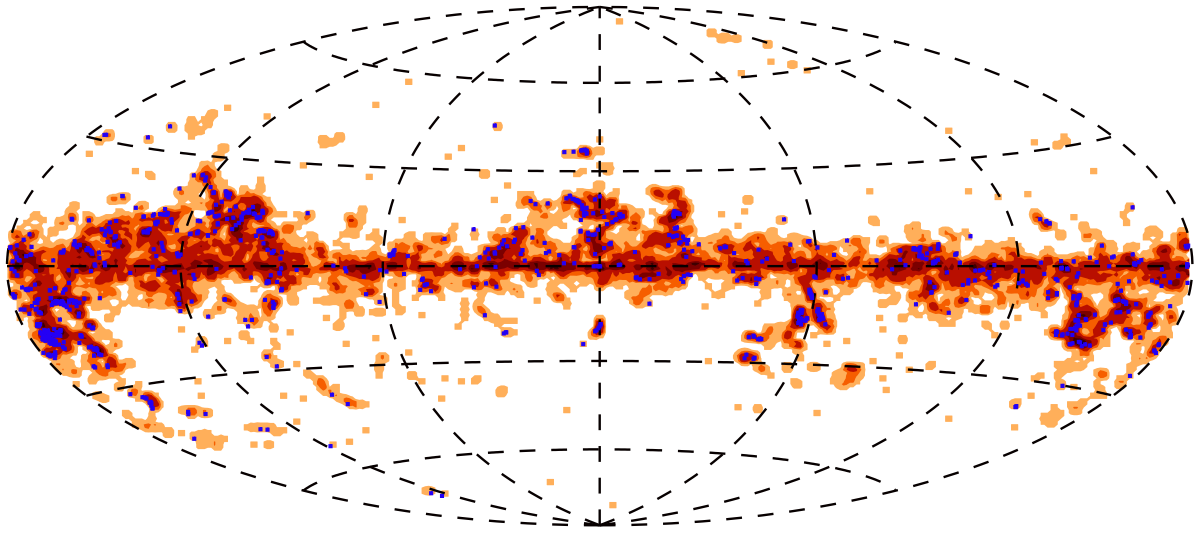


**Fig. 18.** Distribution of the ECC objects (blue squares) over-plotted on the C3PO density all-sky map.

nearby molecular clouds such as Perseus and Taurus, have not been included in this study.

In the restricted coordinate region defined about, there are 802 *Planck* candidate prestellar clumps. We compare the spatial location of these objects using, for the C3PO clumps, the size of the major and minor axis, and the position angles, derived from the fits, as described in Sect. 2.3.1. Likewise, we make use of the same type of information, when provided by the authors, for the rest of the sources. Since at this stage we are only interested in a qualitative, rather than quantitative, analysis, to assess a spatial correlation we simply overlay the positions of the *Planck* sources with those of the other classes of object and count the number of (partial or complete) overlaps between them. In total, we find that 147 *Planck* sources ( $\sim 18\%$ ) appear to be spatially correlated with either the WMAP sources or the SFCs (Fig. 17). Of these, 50 ( $\sim 35\%$ ) candidate cold clumps are located at the edges of the *super-giant* or *giant* shells, while the remaining objects lie within the area delineated by the shells. The relatively low correlation might appear surprising. However, three potentially important caveats should be noted: (1) the WMAP sources are visually identified in the free-free map, hence the completeness of the sample is highly uncertain; (2) likewise for the SFCs, given that they have been extracted with the same technique. In particular, the completeness will be non-uniform across the Galactic plane, with the more confused lines of sight being the most affected by incompleteness; (3) the thickness of the shells traced by the WMAP sources and the SFCs is not provided by the authors. As a consequence, many C3PO clumps which are currently near but not close enough to overlap with the other objects, might actually be found to overlap when the thickness of the *super-giant* and *giant* bubbles is taken into account.

We also do not find a significant spatial correlation with Churchwell et al.'s bubbles. However, in this case, the lack of correlation can be explained by the fact these bubbles and the C3PO sources typically have comparable angular sizes. In fact, often Churchwell et al.'s bubbles are smaller than the *Planck* candidate clumps, suggesting that a triggering scenario in which the formation of a *Planck* clump is induced by the expansion of a GLIMPSE bubble is not very likely.

We strongly emphasize that these results will have to be confirmed by a more detailed and quantitative analysis. In particular, effects due to incompleteness, chance superposition and fore-

ground/background sources along the line of sight will be investigated using Monte Carlo simulations, and information on the distances of all the objects, where available.

## 6. The Early Release Compact Source Catalogue subsample

### 6.1. Selection Criteria

The Early Release Compact Source Catalogue ([Planck Collaboration 2011c](#)) subsample, called the Early Cold Cores (ECC) catalogue, is a subsample of the full C3PO legacy catalogue. It is obtained by applying the following two criteria:

1.  $\text{SNR} > 15$ ,
2.  $T_{\text{ECC}} < 14 \text{ K}$ ,

where SNR is the signal-to-noise ratio of the detection, and  $T_{\text{ECC}}$  is the temperature derived from aperture photometry. However, this temperature  $T_{\text{ECC}}$  is derived differently from the C3PO. In the ECC, the photometry is done on the original *Planck* maps, i.e. maps that still retain the warm component of the diffuse dust emission, by placing an aperture of  $5'$  radius on top of the detection. The background is estimated from an annulus around the aperture with an inner radius of  $5'$  and an outer radius of  $10'$ . Temperature is derived from a fit to all four bands used in the detection. While the annulus is efficient in subtracting the diffuse warm background, any warmer surrounding envelope associated with the cold clump remains. This estimate of the temperature does not take into account the real shape of the sources nor the subtraction of the warm envelope linked to the clump. It does, however, provide a simple and straightforward estimate of the temperature that is used only for the selection process.

The signal-to-noise cut at  $\text{SNR} = 15$  was chosen based on the Monte Carlo Quality Assessment (MCQA) results. a reliability of 90% was required, where the reliability is defined as the fraction of sources that have a recovered flux within 30% of that of the injected sources. The MCQA analysis has shown that the choice of  $\text{SNR} = 15$  ensures a reliability of 90% over the temperature range  $T_{\text{ECC}} < 14 \text{ K}$  in all three *Planck* wavelengths (cf Fig. 23 of [Planck Collaboration 2011v](#)). Hence, the ECC is 90% reliable, where the reliability is based on flux.

These selection criteria lead to a sub-sample of 915 objects over the sky and is distributed as shown in Fig. 18. Of these

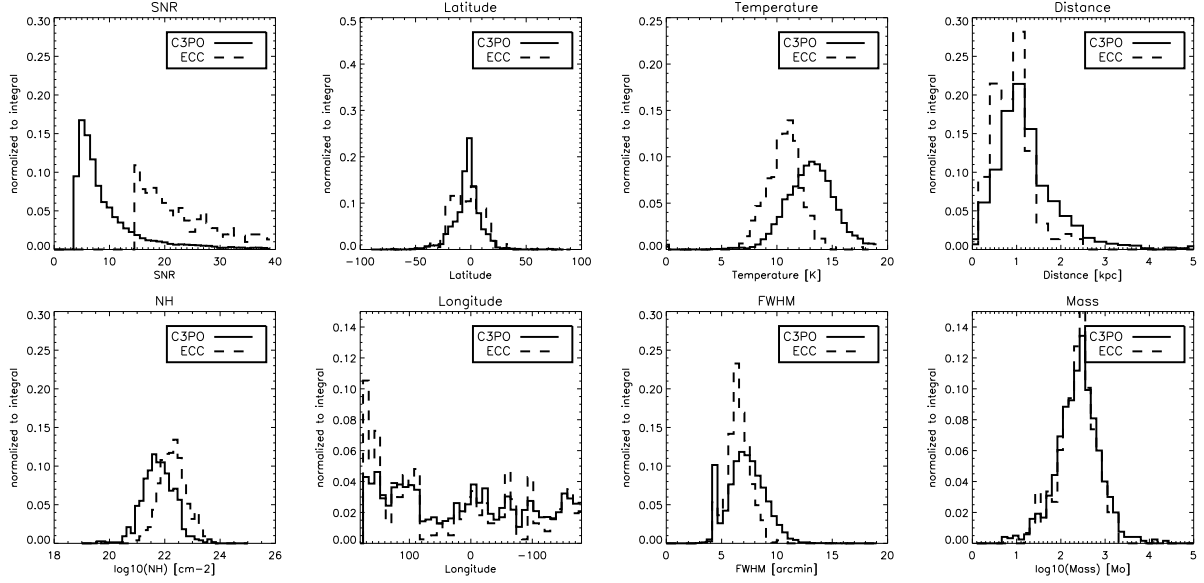


**Fig. 19.** Statistical comparison between ECC and C3PO.

objects 118 have no Simbad entry and are new detections. Thus at least 13% are new detections, as discussed in Sect. 2.5.

### 6.2. Comparison with C3PO catalogue

Fig. 19 shows the histograms of various properties of the C3PO and ECC catalogues, normalized to the integral of each histogram. The selection criteria (high SNR, low temperature) explain the differences between the two catalogues. Because of the SNR selection criteria, the ECC is largely the high SNR tail of C3PO. The clear suppression of objects in the Galactic plane as shown by the latitude histogram is explained by two characteristics of the detections in this region: (1) the plane is warmer and hence CoCoCoDet is able to find less cold objects in the plane; (2) the plane is a confused region, and the SNR tends to be lower than for more isolated sources. The temperature shown in Fig. 19 is not  $T_{\text{ECC}}$  used in the selection criteria, but the derived temperature of the clump itself  $T_{\text{C}}$ . The ECC sources are clearly colder than 14 K as a rule, and even colder than the bulk of the C3PO.

The ECC is clearly weighted towards smaller distances, where SNR is higher due to the flux of the cold clump, while more distant sources have lower SNR. Similar reasons explain the differences in the mass histograms; while the peak is in the same place, the ECC misses very low mass clumps, which have a poor SNR since they are faint, and misses very massive clumps, which tend to be farther away and hence harder to detect. The histograms of hydrogen column density show that ECC is weighted towards sight-lines with higher column density, again due to the temperature. The longitude histograms are complex, but the peak in the direction of the anti-center is caused by the Taurus-Perseus-Aurigae Complex, as also seen on Fig. 18.

Finally, the extent of the clumps, measured here by the full width half maximum of the fitted Gaussian profile, shows that the ECC sources are shifted slightly towards smaller sizes. This can be partly explained by the method of photometry used, but also by the fact that the smaller clumps tend to be colder.

The ECC is not intended to be a complete catalogue, but a subset of high SNR, reliable detections of cold clumps. It is biased towards local, cold objects which have angular sizes comparable to or smaller than the Planck beam.

## 7. Discussion

### 7.1. Nature of the C3PO objects

The C3PO sources have been selected by their colour properties as the relatively coldest Galactic sources over the sky. However their nature is still uncertain: are they cold clouds, clumps or cores? Are they really starless? The low resolution of *Planck* does not allow us to probe the inner structures of these objects to answer these questions. Here we will use the statistical properties discussed in the preceding sections to constrain the nature of the C3PO objects.

The analysis of the mass-luminosity relation (see Sect. 4.5) has shown that 85% of the catalogue display properties of an early stage population, whereas the remaining 15% could be associated with objects that have already started the accretion-powered phase. Thus C3PO sources are mainly pre-stellar objects, but not systematically pre-stellar cores. Table 9 summarizes the properties of the C3PO population in terms of temperature, mass, physical size, molecular column density and density. Following the categorization of Williams et al. (2000) and Bergin & Tafalla (2007) into three populations (clouds, clumps and cores), the *Planck* detections seem mostly associated to clumps and clouds, but not to cores that are defined to be smaller than 0.2 pc, with a density  $n > 10^4 \text{ cm}^{-3}$  and mass  $M < 5 M_{\odot}$ . Indeed a first study based on the prestellar core population revealed by Herschel in Aquila (Könyves et al. 2010) and the *Planck* detections in the same region underlies the fact that *Planck* cold clumps are often associated with at least two Herschel cores. The same question is addressed in more detail in Paper II (Planck Collaboration 2011r), in which a comparison between *Planck* cold clumps maps and higher resolution maps obtained with Herschel follow-up has been performed.

As *Planck* cold clumps are tracing pre-stellar objects, a comparison with IRDC properties is very instructive. A cross-match between C3PO sources and the MSX catalogue of 10931 IRDCs (Simon et al. 2006a) leads to 469 (136 in the *photometric reliable* catalogue) *Planck* Cold Clumps associated with 1007 (296 respectively) MSX IRDCs. Notice also that less than 8% of the *Planck* clumps inside the MSX region are not directly associated with an IRDC, or are located in the border of the spatial

Quantity	min	<>	max
$T_C$ [K]	7	13	17
$N_H$ [ $H_{\text{atom}} \text{ cm}^{-2}$ ]	$10^{20}$	$2 \cdot 10^{21}$	$2 \cdot 10^{23}$
Size [pc]	0.2	1.2	18
Ellipticity	0.4	0.8	1
Mass [ $M_{\odot}$ ]	0.4	88	24000
Mean density [ $\text{cm}^{-3}$ ]	$10^2$	$2 \cdot 10^3$	$10^5$

**Table 9.** Statistical physical properties of the *Planck* C3PO catalogue of cold clumps.

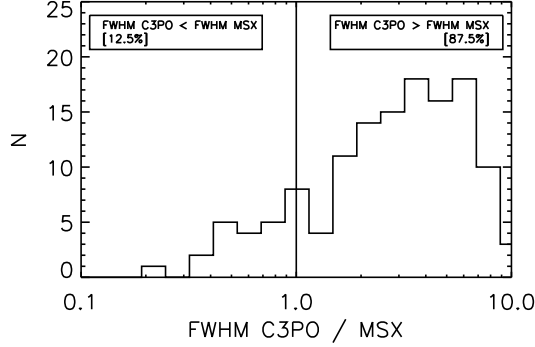


**Fig. 20.** Ratio of the angular extension of C3PO clumps and MSX IRDCs

domain covered by the MSX survey. A comparison of the angular size of these objects is presented on Fig. 20 and clearly shows that the C3PO objects are more extended than the IRDCs, confirming their nature as clumps and not cores. Moreover the fact that most of the IRDCs of Simon et al. (2006a) are themselves divided into cores, gives further evidence of the nature of the *Planck* detections that are only extended clumps.

We also perform a cross-match with the Spitzer catalogue of IRDCs (Peretto & Fuller 2009), leading to 321 (78 on the *photometric reliable* catalogue) *Planck* Cold Clumps associated with 1382 (356 respectively) Spitzer IRDCs. As shown on Fig. 21 C3PO clumps could contains up to 8 MSX IRDCs and 15 Spitzer IRDCs. Moreover, as already stressed in Sect. 4.2, the mean extension of the C3PO sources (about 1.4 times the *Planck* beam) is an indicator of the intrinsic scaling of  $r^{-2}$  for the profile of the extended envelope and an indicator of the physical link between these clumps and the larger scale Galactic diatribution. All these observations favour the fragmentation scenario (Falgaron & Puget 1985; Williams et al. 2000), and place the C3PO objects in the middle of this process, between clouds and cores, as cold sub-structures.

A detailed comparison has been performed on a smaller sample of 14 objects for which a cross-match with MSX IRDCs has been obtained, and providing also kinematic distance, mass and density column estimates (Simon et al. 2006b). Fig. 22 shows the comparison of the mass, column density, density and FWHM. The solid line is the '1:1' relation and the dashed lines show the '1:10' and '1:0.1' relations. As already stressed above, the extension of the C3PO clumps is greater than for IRDCs. The C3PO clumps are 3 to 4 times more massive than the IRDCs, thus the mass of the cores represents only 25% to 30% of the total mass, as observed in the CygX cold core population (Roy et al. 2010). More surprising is that the column density and the density of the clumps are about 2 to 3 times greater than those of the IRDCs. This can be interpreted as a variation of the dust

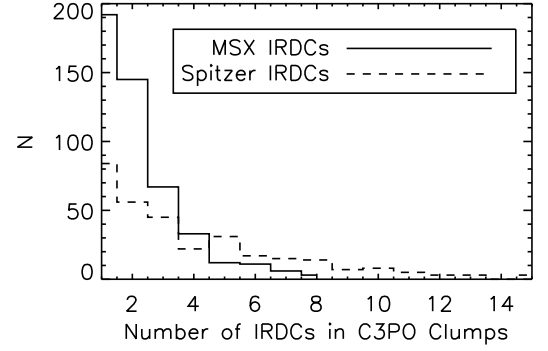


**Fig. 21.** Number of IRDCs found inside the *Planck* Cold Clumps when a match has been obtained with MSX catalogue (Simon et al. 2006a) and Spitzer catalogue (Peretto & Fuller 2009).

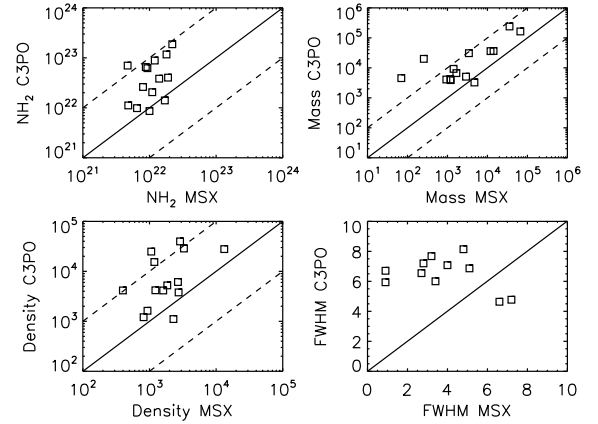


**Fig. 22.** Comparison of the physical properties between 14 sources in common in the C3PO catalogue and the MSX IRDCs, and for which a distance estimate is available.

opacity  $\kappa_v$ , as discussed in Sect. 4.3. We adopted the value of Beckwith et al. (1990) whereas it has been shown that it can vary by a factor of 3 or more from diffuse to dense, cold regions (Ossenkopf & Henning 1994; Kruegel & Siebenmorgen 1994; Stepnik et al. 2003; Juvela et al. 2010). This could partially explain the discrepancy observed here. As an example, the Ossenkopf & Henning (1994) value of  $\kappa_v$  is about twice the estimate of Beckwith et al. (1990) and would tend to lower the observed bias between the column densities of C3PO clumps and MSX IRDCs. However Simon et al. (2001) gave limitations on the column density estimates derived from CO lines that are known to be upper limits and to have an uncertainty of a few. This would then result in acceptable compatibility between C3PO and MSX estimates inside the error bars, without exploring changes of the dust opacity values.

## 7.2. $T, \beta$ relation

The variability of the dust spectral index  $\beta$  is still a contentious issue. Using Pronaos data Dupac et al. (2003) claimed to find an anti-correlation of the dust spectral index with temperature. Since then, many investigations have been carried out on Archeops cold cores (Désert et al. 2008), on Boomerang data (Veneziani et al. 2010) and recently on Herschel data



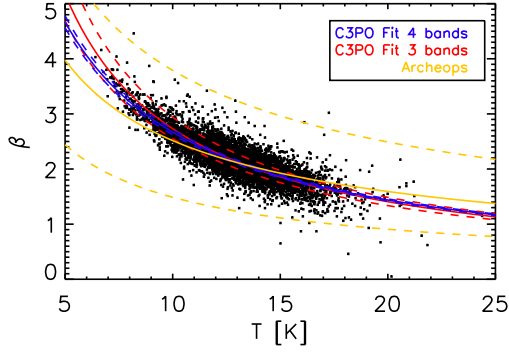


**Fig. 23.** The relation between the temperature and spectral index in the catalogue and the fitted  $\beta(T)$  relations. The estimates are based on bias corrected flux values. The relation estimated from IRAS and the three highest frequency HFI channels is shown in blue line (with  $1\sigma$  error in dashed line), when the red line is the relation obtained using only IRAS and two highest frequency HFI channels. The relation obtained on Archeops cold cores (Désert et al. 2008) is shown in orange.

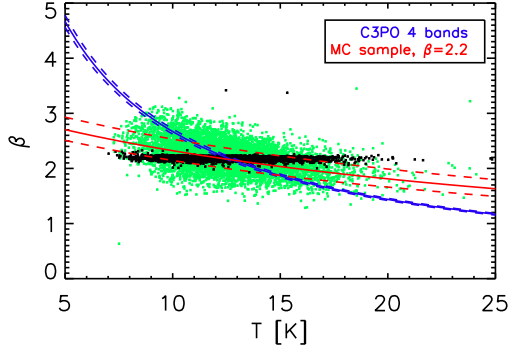


**Fig. 24.** Monte Carlo analysis of the noise effects on the  $\beta(T)$  relation. The black dots correspond to a synthetic sample where the source fluxes have been scaled to be consistent with a constant  $\beta$  value. The green points show the same sources after adding the estimated noise in the flux values, and the red line is the fit to these points. The observed relation (blue line) is significantly steeper.

(Paradis et al. 2010), in which the same behaviour was found. Nevertheless, the issue is not straightforward because the inferred  $T$ - $\beta$  relation suffers from a strong degeneracy between the two parameters.

In the analysis described in this paper, flux values were first corrected for small biases estimated from Monte Carlo simulation. The derived  $(T, \beta)$  values were fitted with a formula

$$\beta = (\delta + \omega T)^{-1}, \quad (17)$$

(see Dupac et al. 2003). Using the IRAS  $100\mu\text{m}$  data and the three highest HFI frequency bands, the least squares fit gave parameters  $\delta = 0.020$  and  $\omega = 0.035$  (see Fig. 23). When the analysis was repeated without the 353 GHz band, the fit gave parameters  $\delta = 0.053$  and  $\omega = 0.032$ . In particular, the presence of the 353 GHz band has only little effect on  $\omega$ , i.e. on the magnitude of the temperature dependence.

To estimate the uncertainty of the parameters, we carried out Monte Carlo simulations starting with the source fluxes. The uncertainties of the flux values were assumed to be 40% for the IRAS  $100\mu\text{m}$  and 8% for the three *Planck* bands. In addition, for each Monte Carlo realization of the catalogue, we included variations in the calibration. The calibration factors were generated from normal distribution and were assumed to be 13.5% for the IRAS observations, 7% for the 545 GHz and 857 GHz and 2% for the 353 GHz *Planck* bands, the same scaling being always applied to the two highest frequency *Planck* bands, as their calibration is based on the correlation with the same FIRAS template (see B). With the estimated statistical uncertainties, the result for the analysis of the four bands is  $\delta = 0.020 \pm 0.001$  and  $\omega = 0.035 \pm 0.001$ .

In addition, we used Monte Carlo simulations to determine to what extent noise could produce an apparent correlation between  $T$  and  $\beta$ . We started with the fluxes, temperatures, and spectral indices listed in the catalogue. For each source, the fluxes were scaled with  $\nu^{2.2-\beta}$  to produce a synthetic sample in which the spectral index is approximately constant but where the deviations from the grey body curve are still consistent with the observed sample. The resulting  $(T, \beta)$  points are plotted in Fig. 24 as black dots. In the Monte-Carlo study, noise is added to the fluxes, and the observed relation is no longer flat (green points and the red least squares line). The scatter of the points is larger than for the observed points (Fig. 23), suggesting that the noise has not been underestimated. Nevertheless, the fitted  $\beta(T)$  curve is still flat compared to the relation observed in the catalogue (blue curve) and the hypothesis of a flat  $\beta(T)$  relation can be excluded with more than 99% confidence.

The recovered temperature dependence of the spectral index is much stronger than the one found in PRONAOS data (Dupac et al. 2003). It is also slightly steeper than the relation reported for Archeops cores (see Fig. 24; Désert et al. 2008) although the Archeops relation is clearly compatible with our results given the uncertainties of the Archeops relation.

This kind of a  $\beta(T)$  relation is expected for amorphous grains with disordered structure (Meny et al. 2007; Boudet et al. 2005). Moreover recent laboratory experiments on silica and silicates have shown a dependence of the spectral index on temperature and wavelength (Coupeaud et al. 2011a,b). As pointed out by Désert et al. (2008), the spectral index is expected to vary also with wavelength and this could have explained part of the difference between PRONAOS at  $200 - 500\mu\text{m}$  and Archeops at longer wavelengths,  $500\mu\text{m} - 2\text{mm}$ . However, with data covering wavelengths from  $100\mu\text{m}$  to  $850\mu\text{m}$ , we also find a very steep  $\beta(T)$  relation. When the spectral index is estimated without our longest wavelength band (353 GHz or  $850\mu\text{m}$ ) the  $\beta(T)$  dependence becomes marginally steeper (see Fig. 23). Although the effect is only slight, it does suggest some flattening of the emission spectrum beyond  $500\mu\text{m}$ .

The observed colour temperature  $T_C$  and spectral index are not identical to the corresponding mass averaged quantities along the line of sight. In the presence of any observational errors, the  $T$  and  $\beta$  parameters become anticorrelated (Schwartz 1982; Dupac et al. 2003). Shetty et al. (2009b,a) studied the effects of both observational noise and line of sight temperature variations on these parameters. The colour temperature is biased towards the warmest regions that emit more radiation. Therefore,  $T_C$  overestimates the real dust temperature and the spectral indices are correspondingly underestimated. With a simple model of two dust layers Shetty et al. (2009a) showed that  $T_C$  may rise above the real dust temperature anywhere along the line of sight. Similar results were obtained by Malinen et al.

(2010) in connection with more complex models that combined magneto-hydrodynamic simulations with radiative transfer modeling. Malinen et al. (2010) concluded that the spectral indices become more biased close to local radiation sources and this could affect the derived  $\beta$ - $T$  relation when the sample also includes star forming clouds. Because of all these effects, some caution is needed when interpreting the value and variation of the observed spectral index. However we see observationally the dust emission spectral index  $\beta$  increasing towards the cold clumps and, because temperature variations tend to decrease  $\beta$  especially towards the clump where the temperature variations are the largest, the actual variations in dust properties may be even more pronounced.

## 8. Conclusion

We have applied a dedicated source extraction algorithm, *CoCoCoDeT* (Montier et al. 2010), to the *Planck* data combined with the IRAS 100  $\mu\text{m}$ , to build a robust catalogue of cold sources over the whole sky. This Cold Core Catalogue of *Planck* Objects (C3PO) is the first objectively selected all-sky catalogue of cold objects. It has been built using the local colour signature of relative colder objects embedded in a warmer background. We stress that this method could lead to missing sources due to an already cold background or spurious warm detections due to very hot backgrounds. The catalogue consists of 10783 objects, from which we have selected the 7608 sources with a complete set of robust physical characteristics such as fluxes, temperature, angular extension, ellipticity and column density. A second sub-sample has been constructed with 2619 sources with distance estimates, physical sizes, masses, and densities. In this paper we have performed a statistical analysis of this complete sample of cold objects and analysed their physical properties.

A dedicated method has been applied to derive the photometry of the clumps themselves, and to look at their local properties inside the warmer envelopes embedded in the Galactic environment. The temperature of the *Planck* cold clumps spans from 7 K to 17 K and peaks at around 13 K, in agreement with previous studies. The advantage of the C3PO catalogue is that it provides a high number of very cold objects, about 600 objects have a temperature  $T_C < 10$  K. It has been shown that the data are not consistent with a constant value of the dust spectral index  $\beta$  over the whole range of temperature. Several possible scenario are possible, such as the effect of multiple temperature components folded into the measurements, and also  $\beta(T)$ . The question of the dependence of the dust spectral index  $\beta$  with temperature has been discussed here and constrained, especially using this low temperature sample. The mean value of  $\beta$  is around 2.1 and  $\beta(T)$  follows a function of the temperature:  $\beta = (\delta + \omega T)^{-1}$  with  $\delta = 0.020$  and  $\omega = 0.035$ . Monte-Carlo simulations have demonstrated that such an anti-correlation can not be explained by a fitting degeneracy given our error bars.

The mean density of these objects varies between  $30 \text{ cm}^{-3}$  and  $10^5 \text{ cm}^{-3}$  with an averaged value of  $2 \times 10^3 \text{ cm}^{-3}$ . Following the prescription of Williams et al. (2000), such objects are classified as clumps, but not cores. The mass range of the catalogue objects varies between 0.3 and  $2.5 \times 10^4 M_\odot$ , the physical sizes span from 0.2 to 18 pc. These parameters of temperature, mass, density and size match well the definition of clumps given by Williams et al. (2000). A cross-match between C3PO sources and IRDCs from MSX and Spitzer has shown that each C3PO cold clump could contain up to 15 IRDCs, and that the C3PO sources are statistically more extended. Thus *Planck* cold detections appear to be mainly cold clumps, intermediate structures of

the fragmentation scenario (Falgarone & Puget 1985), between large clouds and very dense cold cores. Moreover, the fact that they are significantly extended (by a factor of almost 1.4, compared to the PSF of the *Planck*-HFI instrument) indicates that these compact sources are linked to larger envelopes following a power-law profile with index in the range  $-2$  to  $-1$ . These aspects are investigated in further detail in Planck Collaboration (2011r), which analyses Herschel observations of a few *Planck* sources.

The *Planck* cold clump population is strongly associated with Galactic structures, especially the molecular component, and is mainly distributed within the Galactic plane. Nevertheless, as the detection of cold sources inside the thin Galactic plane is difficult due to the high confusion level, most of the detections are located in the Solar neighbourhood, within a distance of 7 kpc. By studying the correlation between the cold clumps and the large scale structures such as the IRAS loops (Könyves et al. 2007) or the WMAP triggering features (Murray & Rahman 2010), it has been shown in this paper that the cold clump population is preferably distributed on the borders of these large shells, where star formation is very active. Another interesting aspect of the C3PO is the filamentary structure of the clumps. This has been statistically quantified over the whole sky and is also apparent in the high degree of ellipticity of the sources. The large variety of objects covered by this all-sky catalogue gives the opportunity to perform a tentative classification using the physical properties, environment, and the evolution stage of these objects. In that perspective, the Herschel follow-up key program Galactic Cold Cores is a unique tool to select a representative sample of cold clumps inside this large C3PO catalogue, and then obtain high resolution information with Herschel-SPIRE/PACS. Such an analysis has already been carried out by Juvela et al. (2010) on Herschel Science Demonstration Phase Data, and is continued in Planck Collaboration (2011r).

Finally, we stress that a robust sub-sample of this large C3PO catalogue has been delivered to the community: the Early Cold Core Catalogue (ECC). It provides a list of 915 objects over the whole sky, with similar statistics at high fluxes to the C3PO, and provides opportunities for ground-based or Herschel follow-up of cold clumps. The final legacy catalogue C3PO will benefit from two further *Planck* sky surveys. It will increase its robustness, via increased redundancy over the sky, and also increase the number of detections because of the reduction of the noise level. The polarization information will be also available in this final version of the catalogue. A special effort will be made to improve the distance estimates and so increase the volume of Galaxy explored, and also to improve the completeness of the statistical analysis.

## Appendix A: Photometry Monte-Carlo Quality Assessment

As presented in Sect. 2.4, we have performed a Monte-carlo Analysis to assess the robustness of the photometry algorithm described in Sect. 2.3. A set of 10000 sources have been injected in *Planck* all-sky maps following a distribution of temperature, dust spectral index and flux in agreement with the observations. Fig. A.1 compiles the relative errors between output and input quantities (fluxes, FWHM, Ellipticity, temperature and spectral index) for the complete set of simulated sources as a function of the flags raised during the photometry estimate. Three flags have been introduced: *Aper Forced* (blue), *Bad Sfit 100  $\mu\text{m}$*  (red) and *Upper 100  $\mu\text{m}$*  (green).

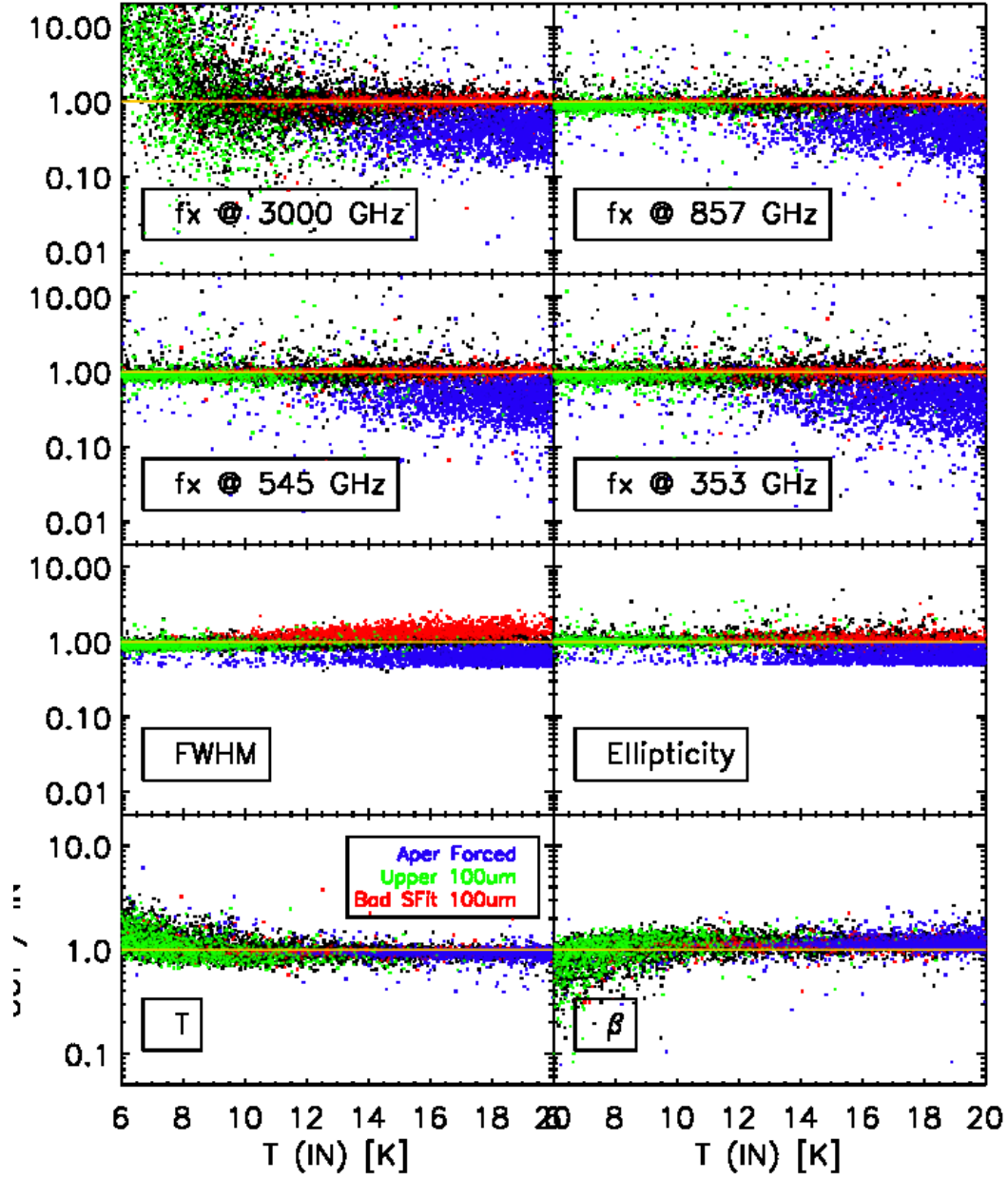


**Fig. A.1.** Comparison of the output and injected values of the Monte-Carlo simulations performed to assess the quality of the photometry algorithm. Black dots refer to the *nominal* case, when red, blue and green dots stand for various flags of the photometry algorithm: *Bad Sfit 100 $\mu$ m*, *Aper Forced* and *Upper 100 $\mu$ m* respectively.

## Appendix B: Impact of Calibration Uncertainty

The calibration uncertainty is known to be 13.5% for the IRIS 100  $\mu$ m (Miville-Deschênes & Lagache 2005), and about 7% for the *Planck* high frequency bands at 857 GHz and 545 GHz, and 2% at 353 GHz (Planck HFI Core Team 2011a). We investigate here what is the impact of this error on temperature and spectral index measurements, considering that it is not independent from one band to the others. The principle is to constrain the 2 top *Planck* bands (545 and 857 GHz) to follow the same relative

calibration error, when the 100  $\mu$ m and the 353 GHz remain independent. For a given temperature  $T$  and a dust spectral index  $\beta$ , SEDs are simulated using a modified black-body modeling, including colour correction. A 13.5% relative noise is added on the 100  $\mu$ m fluxes, when another 7% noise realization is added at 545 GHz and 857 GHz simultaneously, and a 2% noise realization is added on the 353 GHz fluxes. We also study the combination of a calibration error plus an independent error band per band, set to 20% and 10% for 100  $\mu$ m and *Planck* bands respectively. A third set of data is defined as our reference case and



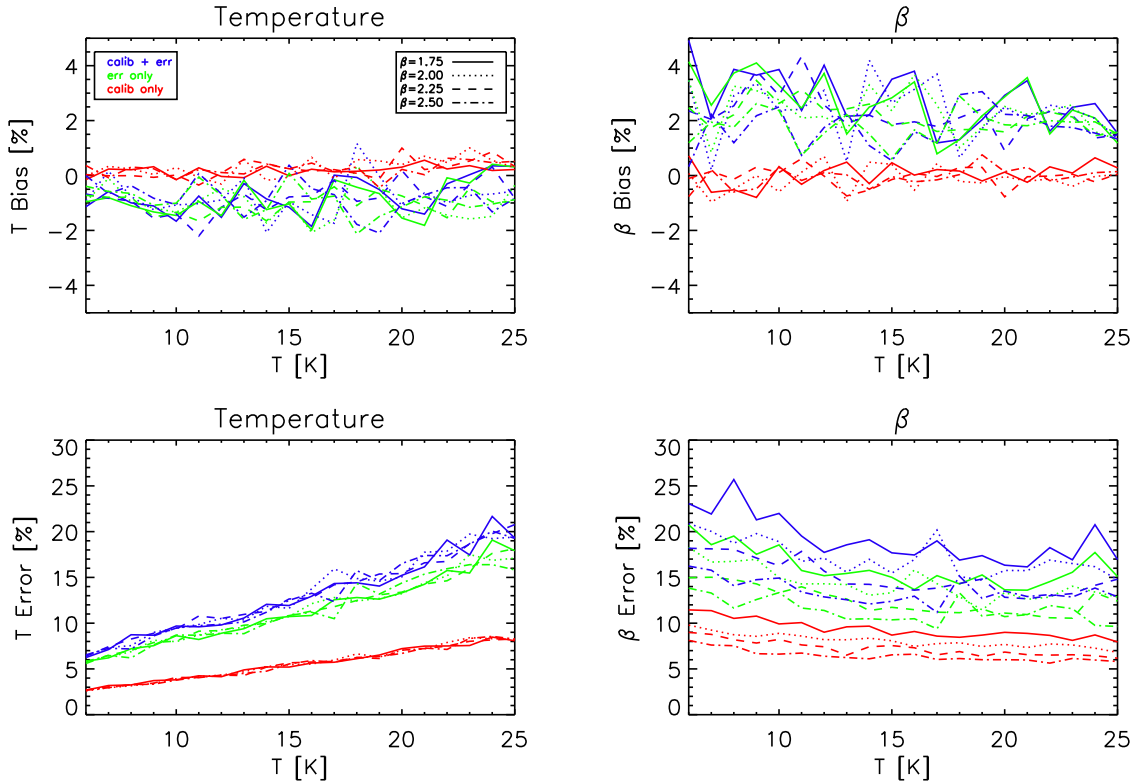


**Fig. B.1.** Bias and  $1\sigma$  discrepancy of the temperature  $T$  and the dust spectral index  $\beta$  estimates derived from a Monte-Carlo analysis dedicated to the study of the impact of the calibration error. three cases have been studied : calibration uncertainty only (red lines), local variance (green) and calibration plus local variance (blue).

does not include any calibration error, but only an independent error per band. The  $T, \beta$  fitting algorithm described in Sect. 4.1 is applied on these 3 sets of SEDs, leading to an estimate of the bias and  $1\sigma$  error of the output distribution, for  $T$  ranging from 6 K to 25 K and  $\beta$  spanning from 1.75 to 2.5.

The results are shown in Fig. B.1. The impact of the calibration uncertainty (in red) is very low compared to the impact of the measurement error only (in green). In all cases, the bias on temperature and  $\beta$  is negligible or significantly lower than 1%. In both cases the bias level remains independent of  $T$  and  $\beta$ . On the other hand the  $1\sigma$  error on the temperature goes from 3% to 8% at respectively 6 K and 25 K due to calibration uncertainty only, and remains independent of  $\beta$ . The  $1\sigma$  discrepancy on  $\beta$  is about 10% to 7% in the temperature range and it decreases of 3% when  $\beta$  goes from 1.75 to 2.5. This error is larger and much more sensitive to  $\beta$  in the case of measurement uncertainty (green curves). Thus the impact of the calibration uncertainty seems very small compared to the impact of the measurement error of the fluxes. Moreover in the case of a combination of calibration and measurement uncertainties (in blue), both resulting uncertainties on  $T$  and  $\beta$  seem to add quadratically.

For this work, we propose to consider separately the impact of the calibration uncertainty, and just add the quadratic errors at the end of the processing. The values of the calibration uncertainties for  $T$  and  $\beta$  are provided in Annex A Table B.1 & B.2 for a given set of  $T, \beta$  parameters.

*Acknowledgements.* A description of the Planck Collaboration and a list of its members can be found at [http://www.rssd.esa.int/index.php?project=PLANCK&page=Planck\\_Collaboration](http://www.rssd.esa.int/index.php?project=PLANCK&page=Planck_Collaboration)

## References

- Aguirre, J. E., Ginsburg, A. G., Dunham, M. K., et al. 2010, ArXiv e-prints  
 Alves, J., Lombardi, M., & Lada, C. J. 2007, A&A, 462, L17  
 André, P., Men'shchikov, A., Bontemps, S., et al. 2010, A&A, 518, L102+  
 Andre, P., Ward-Thompson, D., & Barsony, M. 2000, Protostars and Planets IV, 59  
 Barnard, E. E. 1907, ApJ, 25, 218  
 Beckwith, S. V. W., Sargent, A. I., Chini, R. S., & Guesten, R. 1990, AJ, 99, 924  
 Beemer, I. M., Koenig, X. P., Hora, J. L., et al. 2010, ApJ, 720, 679  
 Benjamin, R. A., Churchwell, E., Babler, B. L., et al. 2003, PASP, 115, 953  
 Bennett, C. L., Halpern, M., Hinshaw, G., et al. 2003, ApJS, 148, 1  
 Bergin, E. A. & Tafalla, M. 2007, ARA&A, 45, 339  
 Bernard, J. P., Abergel, A., Ristorcelli, I., et al. 1999, A&A, 347, 640  
 Bersanelli, M., Mandolesi, N., Butler, R. C., et al. 2010, A&A, 520, A4+  
 Bochanski, J. J., Hawley, S. L., Covey, K. R., et al. 2010, AJ, 139, 2679  
 Bonnor, W. B. 1956, MNRAS, 116, 351  
 Bontemps, S., André, P., Könyves, V., et al. 2010, A&A, 518, L85+  
 Boudet, N., Mutschke, H., Nayral, C., et al. 2005, ApJ, 633, 272  
 Boulanger, F., Abergel, A., Bernard, J., et al. 1996, A&A, 312, 256  
 Cartwright, A. & Whitworth, A. P. 2004, MNRAS, 348, 589  
 Chapin, E. L., Ade, P. A. R., Bock, J. J., et al. 2008, ApJ, 681, 428  
 Charbonneau, P. 1995, apjs, 101, 309, owner: marshall Added to JabRef: 2008.07.29  
 Churchwell, E., Povich, M. S., Allen, D., et al. 2006, ApJ, 649, 759  
 Clemens, D. P., Yun, J. L., & Heyer, M. H. 1991, ApJS, 75, 877  
 Coupeaud, A., Demyk, K., Mény, C., & Nayral, C. 2011a  
 Coupeaud, A., Demyk, K., Mény, C., & Nayral, C. 2011b  
 Covey, K. R., Ivezić, Ž., Schlegel, D., et al. 2007, AJ, 134, 2398  
 Curtis, E. I. & Richer, J. S. 2010, MNRAS, 402, 603  
 Dame, T., Hartmann, D., & Thaddeus, P. 2001, apj, 547, 792, owner: marshall Added to JabRef: 2008.11.12  
 Deharveng, L., Zavagno, A., & Caplan, J. 2005, A&A, 433, 565  
 Désert, F., Macías-Pérez, J. F., Mayet, F., et al. 2008, A&A, 481, 411  
 Dobashi, K. 2011 in preparation  
 Dunham, M. K., Rosolowsky, E., Evans, II, N. J., et al. 2010, ApJ, 717, 1157

T [K]	$\beta = 1.75$		$\beta = 2.00$		$\beta = 2.25$		$\beta = 2.50$	
	Bias [%]	$1 - \sigma$ [%]	Bias [%]	$1 - \sigma$ [%]	Bias [%]	$1 - \sigma$ [%]	Bias [%]	$1 - \sigma$ [%]
6	-0.15	2.68	-0.01	2.59	0.03	2.70	0.36	2.68
7	0.23	3.19	0.34	2.94	-0.01	3.04	-0.08	2.95
8	0.21	3.25	0.24	3.16	-0.00	3.25	0.31	3.29
9	0.32	3.72	0.04	3.41	-0.07	3.44	0.25	3.33
10	-0.15	3.81	0.29	3.92	0.02	4.08	-0.15	3.78
11	0.28	4.25	-0.06	4.17	-0.35	4.04	0.22	4.09
12	-0.03	4.15	-0.31	4.32	0.09	4.32	0.11	4.27
13	-0.08	4.89	0.58	4.69	0.58	4.28	0.06	4.52
14	0.34	5.22	-0.18	5.26	0.43	5.20	0.41	4.76
15	-0.01	5.20	-0.06	5.46	0.25	5.66	0.24	5.54
16	0.23	5.64	0.66	5.54	0.16	5.75	0.45	5.92
17	0.13	5.73	-0.12	5.97	0.21	5.83	0.15	5.74
18	0.16	6.12	0.58	6.64	0.08	6.24	0.31	6.24
19	0.20	6.52	0.53	6.30	-0.12	6.14	-0.45	6.35
20	0.31	7.22	0.40	7.04	1.00	7.05	0.22	6.69
21	0.56	7.49	0.70	7.20	0.22	7.22	0.03	7.28
22	0.24	7.51	0.47	7.89	0.31	7.49	0.63	7.13
23	0.36	7.56	1.01	8.41	0.53	8.02	0.58	8.33
24	0.18	8.48	0.55	8.30	0.87	8.17	0.47	8.56
25	0.22	8.08	0.29	8.21	0.33	8.27	0.51	8.26

**Table B.1.** Bias and  $1 - \sigma$  error on the temperature due to the calibration uncertainty on fluxes in the IRIS 100 $\mu$ m and *Planck* 857, 545 and 353 GHz bands, and estimated for each couple of (T, $\beta$ ).

T [K]	$\beta = 1.75$		$\beta = 2.00$		$\beta = 2.25$		$\beta = 2.50$	
	Bias [%]	$1 - \sigma$ [%]	Bias [%]	$1 - \sigma$ [%]	Bias [%]	$1 - \sigma$ [%]	Bias [%]	$1 - \sigma$ [%]
6	0.72	11.45	0.07	9.79	-0.11	9.00	-0.77	8.12
7	-0.61	11.37	-0.97	9.24	0.15	8.77	0.21	7.61
8	-0.52	10.52	-0.50	8.73	-0.14	8.19	-0.60	7.53
9	-0.80	10.77	0.00	8.56	0.31	7.83	-0.48	6.66
10	0.32	9.91	-0.59	8.89	0.11	8.23	0.29	6.62
11	-0.32	10.06	0.12	8.59	0.61	7.62	-0.18	6.73
12	0.18	9.01	0.70	8.20	-0.02	7.42	0.10	6.39
13	0.49	9.60	-0.95	8.19	-0.74	6.51	0.02	6.24
14	-0.30	9.67	0.49	8.36	-0.53	7.42	-0.50	6.10
15	0.47	8.69	0.41	8.07	-0.15	7.55	-0.04	6.54
16	0.01	9.09	-0.53	7.46	0.08	7.31	-0.23	6.61
17	0.22	8.58	0.43	7.76	-0.04	6.53	-0.16	6.03
18	0.16	8.46	-0.21	7.86	0.29	6.90	0.03	6.13
19	-0.20	8.70	-0.27	7.45	0.30	6.36	0.75	6.01
20	0.12	9.00	-0.04	7.68	-0.78	6.84	0.14	6.01
21	-0.25	8.88	-0.21	7.34	-0.04	6.55	0.30	5.98
22	0.32	8.66	-0.12	7.73	-0.02	6.51	-0.19	5.63
23	0.09	8.12	-0.39	7.62	0.05	6.55	-0.06	6.14
24	0.65	8.71	-0.03	7.27	-0.23	6.44	0.11	5.97
25	0.28	7.95	0.03	6.80	0.06	6.17	0.14	5.81

**Table B.2.** Bias and  $1 - \sigma$  error on the spectral index  $\beta$  due to the calibration uncertainty on fluxes in the IRIS 100 $\mu$ m and *Planck* 857, 545 and 353 GHz bands, and estimated for each couple of (T, $\beta$ ).

Dupac, X., Bernard, J., Boudet, N., et al. 2003, A&A, 404, L11  
Ebert, R. 1955, Zeitschrift für Astrophysik, 37, 217  
Egan, M. P., Shipman, R. F., Price, S. D., et al. 1998, ApJ, 494, L199+  
Elmegreen, B. G. 1998, in Astronomical Society of the Pacific Conference Series, Vol. 148, Origins, ed. C. E. Woodward, J. M. Shull, & H. A. Thronson Jr., 150+  
Elmegreen, B. G. & Falgarone, E. 1996, ApJ, 471, 816  
Enoch, M. L., Glenn, J., Evans, II, N. J., et al. 2007, ApJ, 666, 982  
Enoch, M. L., Young, K. E., Glenn, J., et al. 2006, ApJ, 638, 293  
Falgarone, E. & Puget, J. L. 1985, A&A, 142, 157  
Fischera, J. & Dopita, M. A. 2008, ApJS, 176, 164  
Fukui, Y., Mizuno, N., Yamaguchi, R., et al. 1999, PASJ, 51, 745  
Górski, K. M., Hivon, E., Banday, A. J., et al. 2005, ApJ, 622, 759  
Gutermuth, R. A., Megeath, S. T., Myers, P. C., et al. 2009, ApJS, 184, 18  
Hatchell, J., Richer, J. S., Fuller, G. A., et al. 2005, A&A, 440, 151

Heiles, C. 1979, ApJ, 229, 533  
Heiles, C. 1984, ApJS, 55, 585  
Heiles, C. & Habing, H. J. 1974, A&AS, 14, 1  
Henning, T., Michel, B., & Stognienko, R. 1995, Planet. Space Sci., 43, 1333  
Heyer, M. H., Carpenter, J. M., & Snell, R. L. 2001, ApJ, 551, 852  
Jackson, J., Finn, S., Rathborne, J., Chambers, E., & Simon, R. 2008, apj, 680, 349, owner: marshall Added to JabRef: 2008.07.31  
Juvela, M., Ristorcelli, I., Montier, L. A., et al. 2010, A&A, 518, L93+  
Kauffmann, J., Bertoldi, F., Bourke, T. L., Evans, II, N. J., & Lee, C. W. 2008, A&A, 487, 993  
Kiss, C., Moór, A., & Tóth, L. V. 2004, A&A, 418, 131  
Kiss, Z. T., Tóth, L. V., Balázs, L. G., & Könyves, V. 2006, Publications of the Astronomy Department of the Eotvos Lorand University, 17, 173  
Könyves, V., André, P., Men'shchikov, A., et al. 2010, A&A, 518, L106+

- Konyves, V., Kiss, C., Moor, A., Kiss, Z. T., & Toth, L. V. 2006, *VizieR Online Data Catalog*, 346, 31227
- Könyves, V., Kiss, C., Moór, A., Kiss, Z. T., & Tóth, L. V. 2007, *A&A*, 463, 1227
- Kruegel, E. & Siebenmorgen, R. 1994, *A&A*, 288, 929
- Krumholz, M. R. 2006, *ApJ*, 641, L45
- Krumholz, M. R. & McKee, C. F. 2008, *Nature*, 451, 1082
- Lamarre, J., Puget, J., Ade, P. A. R., et al. 2010, *A&A*, 520, A9+
- Leahy, J. P., Bersanelli, M., D’Arcangelo, O., et al. 2010, *A&A*, 520, A8+
- Malinen, J., Juvela, M., Collins, D. C., Lunttila, T., & Padoan, P. 2010, *ArXiv e-prints*
- Mandolesi, N., Bersanelli, M., Butler, R. C., et al. 2010, *A&A*, 520, A3+
- Marshall, D. J., Joncas, G., & Jones, A. P. 2009, *ArXiv e-prints*
- Marshall, D. J., Robin, A. C., Reylé, C., Schultheis, M., & Picaud, S. 2006, *A&A*, 453, 635
- Mathis, J. S., Mezger, P. G., & Panagia, N. 1983, *A&A*, 128, 212
- Matsunaga, K., Mizuno, N., Moriguchi, Y., et al. 2001, *PASJ*, 53, 1003
- Mc Gehee, P. 2011 in preparation
- Mennella et al. 2011, *Planck early results 03: First assessment of the Low Frequency Instrument in-flight performance* (Submitted to A&A)
- Men’shchikov, A., André, P., Didelon, P., et al. 2010, *A&A*, 518, L103+
- Meny, C., Gromov, V., Boudet, N., et al. 2007, *A&A*, 468, 171
- Mitra, S., Rocha, G., Górski, K. M., et al. 2010, *ArXiv e-prints*
- Miville-Deschênes, M. & Lagache, G. 2005, *ApJS*, 157, 302
- Mizuno, A. & Fukui, Y. 2004, in *Astronomical Society of the Pacific Conference Series*, Vol. 317, *Milky Way Surveys: The Structure and Evolution of our Galaxy*, ed. D. Clemens, R. Shah, & T. Brainerd, 59–+
- Molinari, S., Pezzuto, S., Cesaroni, R., et al. 2008, *A&A*, 481, 345
- Molinari, S., Swinyard, B., Bally, J., et al. 2010, *A&A*, 518, L100+
- Montier, L. A., Pelkonen, V., Juvela, M., Ristorcelli, I., & Marshall, D. J. 2010, *A&A*, 522, A83+
- Motte, F., Andre, P., & Neri, R. 1998, *A&A*, 336, 150
- Murray, N. & Rahman, M. 2010, *ApJ*, 709, 424
- Netterfield, C. B., Ade, P. A. R., Bock, J. J., et al. 2009, *ApJ*, 707, 1824
- Olmi, L., Ade, P. A. R., Anglés-Alcázar, D., et al. 2009, *ApJ*, 707, 1836
- Ossenkopf, V. & Henning, T. 1994, *A&A*, 291, 943
- Pagani, L., Bacmann, A., Motte, F., et al. 2004, *A&A*, 417, 605
- Paradis, D., Veneziani, M., Noriega-Crespo, A., et al. 2010, *A&A*, 520, L8+
- Perauld, M., Omont, A., Simon, G., et al. 1996, *A&A*, 315, L165
- Peretto, N. & Fuller, G. A. 2009, *A&A*, 505, 405
- Planck Collaboration. 2011a, *Planck early results 01: The Planck mission* (Submitted to A&A)
- Planck Collaboration. 2011b, *Planck early results 02: The thermal performance of Planck* (Submitted to A&A)
- Planck Collaboration. 2011c, *Planck early results 07: The Early Release Compact Source Catalogue* (Submitted to A&A)
- Planck Collaboration. 2011d, *Planck early results 08: The all-sky early Sunyaev-Zeldovich cluster sample* (Submitted to A&A)
- Planck Collaboration. 2011e, *Planck early results 09: XMM-Newton follow-up for validation of Planck cluster candidates* (Submitted to A&A)
- Planck Collaboration. 2011f, *Planck early results 10: Statistical analysis of Sunyaev-Zeldovich scaling relations for X-ray galaxy clusters* (Submitted to A&A)
- Planck Collaboration. 2011g, *Planck early results 11: Calibration of the local galaxy cluster Sunyaev-Zeldovich scaling relations* (Submitted to A&A)
- Planck Collaboration. 2011h, *Planck early results 12: Cluster Sunyaev-Zeldovich optical Scaling relations* (Submitted to A&A)
- Planck Collaboration. 2011i, *Planck early results 13: Statistical properties of extragalactic radio sources in the Planck Early Release Compact Source Catalogue* (Submitted to A&A)
- Planck Collaboration. 2011j, *Planck early results 14: Early Release Compact Source Catalogue validation and extreme radio sources* (Submitted to A&A)
- Planck Collaboration. 2011k, *Planck early results 15: Spectral energy distributions and radio continuum spectra of northern extragalactic radio sources* (Submitted to A&A)
- Planck Collaboration. 2011l, *Planck early results 16: The Planck view of nearby galaxies* (Submitted to A&A)
- Planck Collaboration. 2011m, *Planck early results 17: Origin of the submillimetre excess dust emission in the Magellanic Clouds* (Submitted to A&A)
- Planck Collaboration. 2011n, *Planck early results 18: The power spectrum of cosmic infrared background anisotropies* (Submitted to A&A)
- Planck Collaboration. 2011o, *Planck early results 19: All-sky temperature and dust optical depth from Planck and IRAS — constraints on the “dark gas” in our Galaxy* (Submitted to A&A)
- Planck Collaboration. 2011p, *Planck early results 20: New light on anomalous microwave emission from spinning dust grains* (Submitted to A&A)
- Planck Collaboration. 2011q, *Planck early results 21: Properties of the interstellar medium in the Galactic plane* (Submitted to A&A)
- Planck Collaboration. 2011r, *Planck early results 22: The submillimetre properties of a sample of Galactic cold clumps* (Submitted to A&A)
- Planck Collaboration. 2011s, *Planck early results 23: The Galactic cold core population revealed by the first all-sky survey* (Submitted to A&A)
- Planck Collaboration. 2011t, *Planck early results 24: Dust in the diffuse interstellar medium and the Galactic halo* (Submitted to A&A)
- Planck Collaboration. 2011u, *Planck early results 25: Thermal dust in nearby molecular clouds* (Submitted to A&A)
- Planck Collaboration. 2011v, *The Explanatory Supplement to the Planck Early Release Compact Source Catalogue* (ESA)
- Planck HFI Core Team. 2011a, *Planck early results 04: First assessment of the High Frequency Instrument in-flight performance* (Submitted to A&A)
- Planck HFI Core Team. 2011b, *Planck early results 06: The High Frequency Instrument data processing* (Submitted to A&A)
- Preibisch, T., Ossenkopf, V., Yorke, H. W., & Henning, T. 1993, *A&A*, 279, 577
- Rahman, M. & Murray, N. 2010, *ApJ*, 719, 1104
- Rathborne, J. M., Jackson, J. M., Chambers, E. T., et al. 2010, *ApJ*, 715, 310
- Rathborne, J. M., Jackson, J. M., & Simon, R. 2006, *ApJ*, 641, 389
- Rathborne, J. M., Lada, C. J., Muench, A. A., Alves, J. F., & Lombardi, M. 2008, *ApJS*, 174, 396
- Robin, A., Reylé, C., Derrière, S., & Picaud, S. 2003, *aap*, 409, 523, owner: marshall Added to JabRef: 2008.07.29
- Rosset, C., Tristram, M., Ponthieu, N., et al. 2010, *A&A*, 520, A13+
- Roy, A., Ade, P. A. R., Bock, J. J., et al. 2010, *ArXiv e-prints*
- Schlaflly, E. F., Finkbeiner, D. P., Schlegel, D. J., et al. 2010, *ApJ*, 725, 1175
- Schlegel, D. J., Finkbeiner, D. P., & Davis, M. 1998, *ApJ*, 500, 525
- Schmeja, S. & Klessen, R. S. 2006, *A&A*, 449, 151
- Schwartz, P. R. 1982, *ApJ*, 252, 589
- Shetty, R., Kauffmann, J., Schnee, S., & Goodman, A. A. 2009a, *ApJ*, 696, 676
- Shetty, R., Kauffmann, J., Schnee, S., Goodman, A. A., & Ercolano, B. 2009b, *ApJ*, 696, 2234
- Simon, R., Jackson, J. M., Clemens, D. P., Bania, T. M., & Heyer, M. H. 2001, *ApJ*, 551, 747
- Simon, R., Jackson, J. M., Rathborne, J. M., & Chambers, E. T. 2006a, *ApJ*, 639, 227
- Simon, R., Rathborne, J. M., Shah, R. Y., Jackson, J. M., & Chambers, E. T. 2006b, *ApJ*, 653, 1325
- Skrutskie, M., Cutri, R., Stiening, R., et al. 2006, *aj*, 131, 1163, owner: marshall Added to JabRef: 2008.07.29
- Stepnik, B., Abergel, A., Bernard, J., et al. 2003, *A&A*, 398, 551
- Tauber, J. A., Mandolesi, N., Puget, J., et al. 2010, *A&A*, 520, A1+
- Tóth, L. V. & Kiss, Z. T. 2007, in *IAU Symposium*, Vol. 237, *IAU Symposium*, ed. B. G. Elmegreen & J. Palous, 124–127
- Veneziani, M., Ade, P. A. R., Bock, J. J., et al. 2010, *ApJ*, 713, 959
- Ward-Thompson, D., Kirk, J. M., André, P., et al. 2010, *A&A*, 518, L92+
- Weaver, H. & Williams, D. R. W. 1973, *A&AS*, 8, 1
- Wheelock, S. L., Gautier, T. N., Chillemi, J., et al. 1994, *NASA STI/Recon Technical Report N*, 95, 22539
- Williams, J. P., Blitz, L., & McKee, C. F. 2000, in *Protostars and Planets IV*, ed. V. Mannings, A. P. Boss, & S. S. Russell, University of Arizona Press, 97
- Young, C. H., Shirley, Y. L., Evans, II, N. J., & Rawlings, J. M. C. 2003, *ApJS*, 145, 111
- Young, K. E., Enoch, M. L., Evans, II, N. J., et al. 2006, *ApJ*, 644, 326
- Zacchei et al. 2011, *Planck early results 05: The Low Frequency Instrument data processing* (Submitted to A&A)
- Zavagno, A., Anderson, L. D., Russeil, D., et al. 2010a, *A&A*, 518, L101+
- Zavagno, A., Russeil, D., Motte, F., et al. 2010b, *A&A*, 518, L81+

<sup>1</sup> Aalto University Metsähovi Radio Observatory, Metsähovintie 114, FIN-02540 Kylmälä, Finland

<sup>2</sup> Agenzia Spaziale Italiana Science Data Center, c/o ESRIN, via Galileo Galilei, Frascati, Italy

<sup>3</sup> Astroparticule et Cosmologie, CNRS (UMR7164), Université Denis Diderot Paris 7, Bâtiment Condorcet, 10 rue A. Domon et Léonie Duquet, Paris, France

<sup>4</sup> Atacama Large Millimeter/submillimeter Array, ALMA Santiago Central Offices Alonso de Cordova 3107, Vitacura, Casilla 763 0355, Santiago, Chile

<sup>5</sup> CITA, University of Toronto, 60 St. George St., Toronto, ON M5S 3H8, Canada



- <sup>6</sup> CNRS, IRAP, 9 Av. colonel Roche, BP 44346, F-31028 Toulouse cedex 4, France
- <sup>7</sup> California Institute of Technology, Pasadena, California, U.S.A.
- <sup>8</sup> DAMTP, Centre for Mathematical Sciences, Wilberforce Road, Cambridge CB3 0WA, U.K.
- <sup>9</sup> DSM/Irfu/SPP, CEA-Saclay, F-91191 Gif-sur-Yvette Cedex, France
- <sup>10</sup> DTU Space, National Space Institute, Juliane Mariesvej 30, Copenhagen, Denmark
- <sup>11</sup> Département de physique, de génie physique et d'optique, Université Laval, Québec, Canada
- <sup>12</sup> Departamento de Física, Universidad de Oviedo, Avda. Calvo Sotelo s/n, Oviedo, Spain
- <sup>13</sup> Department of Astronomy and Astrophysics, University of Toronto, 50 Saint George Street, Toronto, Ontario, Canada
- <sup>14</sup> Department of Astronomy and Earth Sciences, Tokyo Gakugei University, Koganei, Tokyo 184-8501, Japan
- <sup>15</sup> Department of Physics & Astronomy, University of British Columbia, 6224 Agricultural Road, Vancouver, British Columbia, Canada
- <sup>16</sup> Department of Physics, Gustaf Hållströmin katu 2a, University of Helsinki, Helsinki, Finland
- <sup>17</sup> Department of Physics, Princeton University, Princeton, New Jersey, U.S.A.
- <sup>18</sup> Department of Physics, Purdue University, 525 Northwestern Avenue, West Lafayette, Indiana, U.S.A.
- <sup>19</sup> Department of Physics, University of California, Berkeley, California, U.S.A.
- <sup>20</sup> Department of Physics, University of California, One Shields Avenue, Davis, California, U.S.A.
- <sup>21</sup> Department of Physics, University of California, Santa Barbara, California, U.S.A.
- <sup>22</sup> Department of Physics, University of Illinois at Urbana-Champaign, 1110 West Green Street, Urbana, Illinois, U.S.A.
- <sup>23</sup> Dipartimento di Fisica G. Galilei, Università degli Studi di Padova, via Marzolo 8, 35131 Padova, Italy
- <sup>24</sup> Dipartimento di Fisica, Università La Sapienza, P. le A. Moro 2, Roma, Italy
- <sup>25</sup> Dipartimento di Fisica, Università degli Studi di Milano, Via Celoria, 16, Milano, Italy
- <sup>26</sup> Dipartimento di Fisica, Università degli Studi di Trieste, via A. Valerio 2, Trieste, Italy
- <sup>27</sup> Dipartimento di Fisica, Università di Roma Tor Vergata, Via della Ricerca Scientifica, 1, Roma, Italy
- <sup>28</sup> Discovery Center, Niels Bohr Institute, Blegdamsvej 17, Copenhagen, Denmark
- <sup>29</sup> Dpto. Astrofísica, Universidad de La Laguna (ULL), E-38206 La Laguna, Tenerife, Spain
- <sup>30</sup> Eötvös Loránd University, Department of Astronomy, Pázmány Péter sétány 1/A, 1117 Budapest, Hungary
- <sup>31</sup> European Southern Observatory, ESO Vitacura, Alonso de Cordova 3107, Vitacura, Casilla 19001, Santiago, Chile
- <sup>32</sup> European Space Agency, ESAC, Planck Science Office, Camino bajo del Castillo, s/n, Urbanización Villafranca del Castillo, Villanueva de la Cañada, Madrid, Spain
- <sup>33</sup> European Space Agency, ESTEC, Keplerlaan 1, 2201 AZ Noordwijk, The Netherlands
- <sup>34</sup> Helsinki Institute of Physics, Gustaf Hållströmin katu 2, University of Helsinki, Helsinki, Finland
- <sup>35</sup> INAF - Osservatorio Astrofisico di Catania, Via S. Sofia 78, Catania, Italy
- <sup>36</sup> INAF - Osservatorio Astronomico di Padova, Vicolo dell'Osservatorio 5, Padova, Italy
- <sup>37</sup> INAF - Osservatorio Astronomico di Roma, via di Frascati 33, Monte Porzio Catone, Italy
- <sup>38</sup> INAF - Osservatorio Astronomico di Trieste, Via G.B. Tiepolo 11, Trieste, Italy
- <sup>39</sup> INAF/IASF Bologna, Via Gobetti 101, Bologna, Italy
- <sup>40</sup> INAF/IASF Milano, Via E. Bassini 15, Milano, Italy
- <sup>41</sup> INRIA, Laboratoire de Recherche en Informatique, Université Paris-Sud 11, Bâtiment 490, 91405 Orsay Cedex, France
- <sup>42</sup> IPAG: Institut de Planétologie et d'Astrophysique de Grenoble, Université Joseph Fourier, Grenoble 1 / CNRS-INSU, UMR 5274, Grenoble, F-38041, France
- <sup>43</sup> Imperial College London, Astrophysics group, Blackett Laboratory, Prince Consort Road, London, SW7 2AZ, U.K.
- <sup>44</sup> Infrared Processing and Analysis Center, California Institute of Technology, Pasadena, CA 91125, U.S.A.
- <sup>45</sup> Institut d'Astrophysique Spatiale, CNRS (UMR8617) Université Paris-Sud 11, Bâtiment 121, Orsay, France
- <sup>46</sup> Institut d'Astrophysique de Paris, CNRS UMR7095, Université Pierre & Marie Curie, 98 bis boulevard Arago, Paris, France
- <sup>47</sup> Institute of Astronomy and Astrophysics, Academia Sinica, Taipei, Taiwan
- <sup>48</sup> Institute of Theoretical Astrophysics, University of Oslo, Blindern, Oslo, Norway
- <sup>49</sup> Instituto de Astrofísica de Canarias, C/Vía Láctea s/n, La Laguna, Tenerife, Spain
- <sup>50</sup> Instituto de Física de Cantabria (CSIC-Universidad de Cantabria), Avda. de los Castros s/n, Santander, Spain
- <sup>51</sup> Jet Propulsion Laboratory, California Institute of Technology, 4800 Oak Grove Drive, Pasadena, California, U.S.A.

- <sup>52</sup> Jodrell Bank Centre for Astrophysics, Alan Turing Building, School of Physics and Astronomy, The University of Manchester, Oxford Road, Manchester, M13 9PL, U.K.
- <sup>53</sup> Kavli Institute for Cosmology Cambridge, Madingley Road, Cambridge, CB3 0HA, U.K.
- <sup>54</sup> LERMA, CNRS, Observatoire de Paris, 61 Avenue de l'Observatoire, Paris, France
- <sup>55</sup> Laboratoire AIM, IRFU/Service d'Astrophysique - CEA/DSM - CNRS - Université Paris Diderot, Bât. 709, CEA-Saclay, F-91191 Gif-sur-Yvette Cedex, France
- <sup>56</sup> Laboratoire Traitement et Communication de l'Information, CNRS (UMR 5141) and Télécom ParisTech, 46 rue Barrault F-75634 Paris Cedex 13, France
- <sup>57</sup> Laboratoire de Physique Subatomique et de Cosmologie, CNRS, Université Joseph Fourier Grenoble I, 53 rue des Martyrs, Grenoble, France
- <sup>58</sup> Laboratoire de l'Accélérateur Linéaire, Université Paris-Sud 11, CNRS/IN2P3, Orsay, France
- <sup>59</sup> Lawrence Berkeley National Laboratory, Berkeley, California, U.S.A.
- <sup>60</sup> Max-Planck-Institut für Astrophysik, Karl-Schwarzschild-Str. 1, 85741 Garching, Germany
- <sup>61</sup> MilliLab, VTT Technical Research Centre of Finland, Tietotie 3, Espoo, Finland
- <sup>62</sup> National University of Ireland, Department of Experimental Physics, Maynooth, Co. Kildare, Ireland
- <sup>63</sup> Niels Bohr Institute, Blegdamsvej 17, Copenhagen, Denmark
- <sup>64</sup> Observational Cosmology, Mail Stop 367-17, California Institute of Technology, Pasadena, CA, 91125, U.S.A.
- <sup>65</sup> Optical Science Laboratory, University College London, Gower Street, London, U.K.
- <sup>66</sup> SISSA, Astrophysics Sector, via Bonomea 265, 34136, Trieste, Italy
- <sup>67</sup> SUPA, Institute for Astronomy, University of Edinburgh, Royal Observatory, Blackford Hill, Edinburgh EH9 3HJ, U.K.
- <sup>68</sup> School of Physics and Astronomy, Cardiff University, Queens Buildings, The Parade, Cardiff, CF24 3AA, U.K.
- <sup>69</sup> Space Sciences Laboratory, University of California, Berkeley, California, U.S.A.
- <sup>70</sup> Spitzer Science Center, 1200 E. California Blvd., Pasadena, California, U.S.A.
- <sup>71</sup> Stanford University, Dept of Physics, Varian Physics Bldg, 382 Via Pueblo Mall, Stanford, California, U.S.A.
- <sup>72</sup> Université de Toulouse, UPS-OMP, IRAP, F-31028 Toulouse cedex 4, France
- <sup>73</sup> Universities Space Research Association, Stratospheric Observatory for Infrared Astronomy, MS 211-3, Moffett Field, CA 94035, U.S.A.
- <sup>74</sup> University of Cambridge, Cavendish Laboratory, Astrophysics group, J J Thomson Avenue, Cambridge, U.K.
- <sup>75</sup> University of Cambridge, Institute of Astronomy, Madingley Road, Cambridge, U.K.
- <sup>76</sup> University of Granada, Departamento de Física Teórica y del Cosmos, Facultad de Ciencias, Granada, Spain
- <sup>77</sup> University of Miami, Knight Physics Building, 1320 Campo Sano Dr., Coral Gables, Florida, U.S.A.
- <sup>78</sup> Warsaw University Observatory, Aleje Ujazdowskie 4, 00-478 Warszawa, Poland